

Universiteit
Leiden
The Netherlands

Breathing in thin air: structure, function and therapeutic opportunities of bd type oxidases

Velden, T.T. van der

Citation
Velden, T. T. van der. (2026, September 2). *Breathing in thin air: structure, function and therapeutic opportunities of bd type oxidases*. Retrieved from https://hdl.handle.net/1887/4309020

Version:	Publisher's Version
License:	Licence agreement concerning inclusion of doctoral thesis in the Institutional Repository of the University of Leiden
Downloaded from:	https://hdl.handle.net/1887/4309020

Note: To cite this publication please use the final published version (if applicable).

Chapter 3

Visualizing the mechanism of quinol oxidation and inhibition of a *bd*-type oxidase using cryo-EM

Cytochrome *bd* is a prokaryotic terminal oxidase recognized as an antibiotic target against various pathogens. Despite its critical role in respiration, failure to capture the mechanism of quinol oxidation and inhibition prohibits structure guided drug discovery. Here, we present cryo-electron microscopy structures of *Escherichia coli* cytochrome *bd*-I in monomeric and dimeric forms, in several quinone and inhibitor-bound states. We identify a dynamic Q-loop lid that undergoes a disorder-to-order transition upon substrate binding to the dimer, completing the active site and enabling catalysis. Structure-guided mutagenesis confirms $Tyr243^{CydA}$ and $Arg298^{CydA}$ as conserved catalytic residues unique to long Q-loop oxidases, highlighting evolutionary divergence from other subfamilies. Inhibition by Aurachin D triggers refolding of the active site, occluding substrate access via an $Asp239^{CydA}$-mediated mechanism. The structural and mechanistic insights presented here establish a comprehensive framework, opening paths for drug discovery against *bd* oxidases.

Tijn T. van der Velden
Kanwal Kayastha
Famke Pelser
Steffen Brünle
Lars J.C. Jeuken
Science advances, DOI: 10.1126/sciadv.aec9946

Introduction

The bacterial respiratory chain has emerged as a promising target for next-generation antibiotics due to its essential role in ATP generation[153]. Disruption of this pathway has proven effective in eliminating pathogens resistant to conventional therapeutics, as demonstrated by the clinical success of bedaquiline, an ATP synthase inhibitor approved for the treatment of multidrug-resistant tuberculosis[63]. Among the terminal oxidases, cytochrome *bd* (cyt *bd*) is characterized by an exceptionally high oxygen affinity and ability to confer resistance to oxidative stress and tolerance against diverse antibiotics [46–48,56,59,154]. This enables pathogens to sustain respiration under hostile conditions encountered during infection. Notably, cyt *bd* is absent in eukaryotes, making it an attractive target for selective antimicrobial development against pathogens such as *Mycobacterium tuberculosis* [77], *Salmonella enterica* [155], pathogenic *Escherichia coli* [78], and *Staphylococcus aureus* [156].

Cyt *bd* catalyzes the reduction of molecular oxygen to water using electrons from the quinone pool. During this turnover, cyt *bd* releases the chemical protons associated with quinol oxidation to the periplasm while capturing cytoplasmic protons for oxygen reduction, thereby contributing four protons per oxygen reduced to the proton motive force required for ATP synthesis (Fig. 3.1A,B). The canonical enzyme architecture comprises two core subunits, CydA and CydB, and in some species, auxiliary subunits such as CydS, CydX, and CydH[81,83]. CydA harbors the three heme cofactors, b_{558}, b_{595}, and *d*, as well as the putative quinone binding site near the Q-loop, a flexible periplasmic region adjacent to heme b_{558}[83]. The cyt *bd* oxidase family of enzymes has been phylogenetically classified into qOR, OR-C and OR-N subfamilies. The cyt *bd* oxidases with a quinol binding site in CydA belong to the qOR subfamily, which are further subdivided into qOR1, qOR2, qOR3 and qOR4a[88], where qOR1 forms the major cluster. The qOR1 family can be further subdivided into long and short Q-loop subfamilies based on the presence of a C-terminal Q-loop extension found in the proteobacterial clade, though the functional implications of the phylogenetic divergence remain unresolved[89,90].

E. coli cyt *bd-I* (*Ecbd*), representative of the qOR1 long Q-loop subfamily, consist of the four subunits CydA, CydB, CydX and CydH. The available substrate pool in *E. coli* consists of three quinone subtypes, ubiquinone (UQ), demethylmenaquinone (DMK) and menaquinone (MK). The composition of this quinone pool adapts based on the environmental oxygen concentration, switching from predominantly UQ to MK under micro-aerobic conditions when *Ecbd* is expressed[18]. Despite extensive characterization[83,86,91], structural and mechanistic insights into the quinol oxidation and inhibition mechanism of cyt *bd* have remained elusive.

To gain insights into quinone turnover and inhibition of *bd*-type oxidases, we have resolved cryo-EM structures of *Ecbd* in its unbound, MK bound and inhibitor bound state. We identified both monomeric and dimeric forms of *Ecbd*, with the latter exhibiting increased catalytic activity. The dimeric form revealed three discrete quinone binding sites per protomer. In the quinol oxidation site, located near heme b_{558}, MK was observed to occupy a cavity formed by a disorder-to-order transition of the Q-loop lid. Unexpectedly, the quinol oxidation site undergoes a structural rearrangement upon binding of the inhibitor Aurachin D, occluding the quinone from binding to its pocket. Utilizing these structures, site directed mutagenesis, enzyme kinetics, and sequence analysis we propose the catalytic cycle of *Ecbd*, and underline critical structural features required for quinol turnover and inhibition.

Results

Purification and structure determination of Ecbd

Ecbd was expressed in MB43 cells and purified using affinity chromatography followed by gel filtration using the detergent Lauryl Maltose Neopentyl Glycol (LMNG). To gain insights into the turnover mechanism of *Ecbd*, we determined cryo-EM structures in LMNG and observed heterogeneity on the grid. 3D classification of the as-isolated sample resulted in the structures without MK (I, unbound) and with MK (II, bound). Within the MK bound structures, open and closed states were observed (II, bound^{open}; III, bound^{closed}). To further improve

the resolution of state (III), *Ecbd* was reconstituted into phosphatidylcholine (PC) nanodiscs doped with 5% MK-9 (product). Last, incubation of *Ecbd* with AurD in LMNG resulted in the inhibitor bound state (IV). The different structures and samples conditions are shown in Fig. 3.1C, Table S3.1, and Fig. S3.1-4.

Our cryo-EM analysis identified previously uncharacterized dimeric forms of *Ecbd,* potentially due to the mild solubilization with LMNG, which mirrored the dimeric structure of the homolog *E. coli cyt bd*-II[87]. The dimeric states of *Ecbd* (I), (II), (III), and (IV) were resolved at 2.2-2.5 Å overall resolution. Additionally, on the same grids, the canonical monomeric architecture for sample (I), (II), and (IV) were resolved at 2.4-2.6 Å overall resolution (Fig. S3.5). However, all three monomeric structures show an identical state, with no additional ligand binding being observed other than a structural quinone in CydB. Consistent with previous reports[83] *Ecbd* adopts a heterotetrameric architecture that consists of the subunits CydA, CydB, CydX and CydH (Fig. 3.1D). CydA forms the catalytic core, harboring the three heme cofactors (b_{558}, b_{595}, and d) and the putative quinone-binding Q-loop required for oxidase activity (Fig. 3.1B). In contrast to previous reports, our high resolution cryo-EM map indicates that the heme *d* hydroxychlorin γ-spirolactone exists in the trans rather than the cis orientation (Fig. S3.6). This trans orientation is further confirmed by prior NMR and IR analysis of the isolated heme[157], and positions the spirolactone group opposite the bound dioxygen molecule. Close examination of prior cyt *bd* density maps indicates the possibility of a more general trans heme *d* orientation within the *bd*-oxidase family, although unambiguous assignment of the chirality remains challenging due to limitations in resolution.

The *Ecbd* dimer consists of 20 transmembrane helices existing in a symmetrical architecture around the CydX dimer interface (Fig. 3.1E). CydX forms hydrophobic contacts with CydA helix 1, 5, and 6 to connect the two protomers together. To confirm the physiological relevance of both monomer and dimeric states, *Ecbd* was extracted from the membrane using styrene-maleic acid lipid particles (SMALPs). Cryo-EM imaging followed by 2D classification showed clear populations consisting of dimeric and monomeric particles, indicating the existence of both oligomeric states *in vivo* (Fig. S3.7).

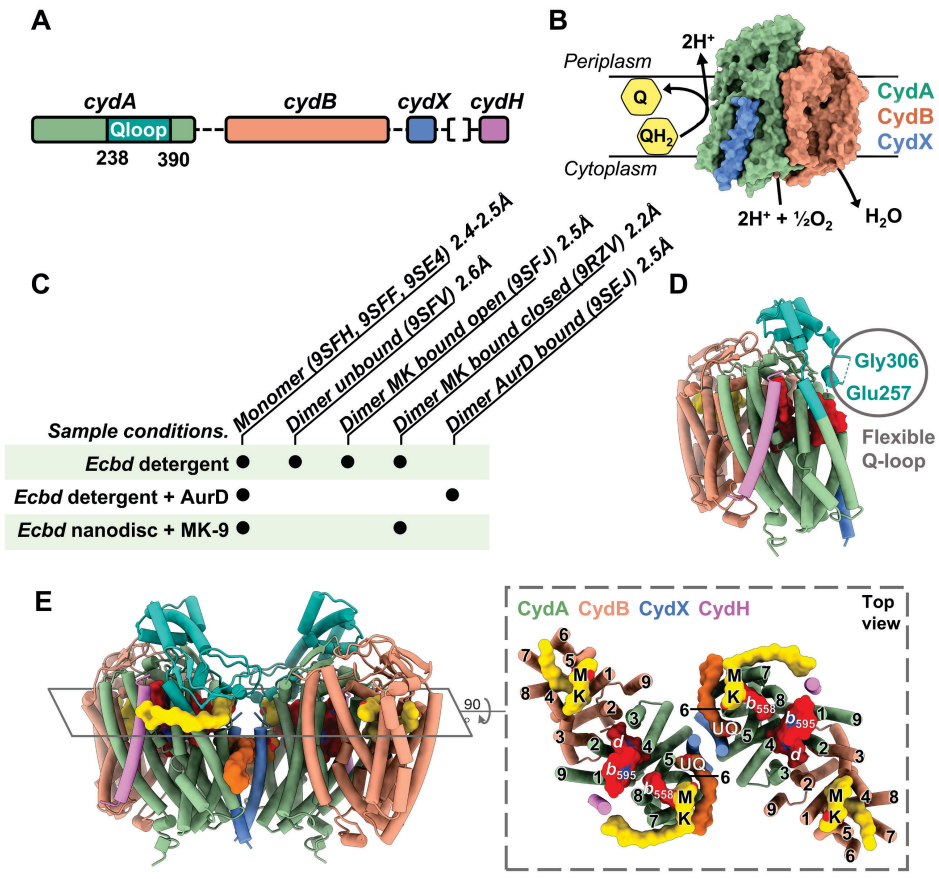


Fig. 3.1. Overview of the structures and function of *Ecbd*. (**A**) Genomic organization of the *Ecbd* subunits. Subunit CydH originates from a different operon than the other *Ecbd* subunits. (**B**) Schematic oxidase activity of *Ecbd*. (**C**) Overview of the different sample conditions used to yield the presented monomer and dimeric states presented, including their state and resolution. PDB 9RZV was resolved from the nanodisc sample. (**D**) Structural overview of the *Ecbd* monomer. CydA is shown in green, with the Q-loop in cyan, CydB in orange, CydX in blue, CydH in purple. (**E**) Structural overview of the *Ecbd* dimer in the MK bound state with the Q-loop highlighted. MK is shown yellow and UQ In dark orange. The right shows a cross section of the *Ecbd* dimer with a total of 40 transmembrane helices, highlighting all identified MK (yellow) and UQ (dark orange), as well as heme groups (red).

Both oligomeric states contained tightly bound phospholipids at the protein periphery and dimer interface (Fig. S3.8). Lipids lacking discernible headgroups were modeled as phosphatidic acid, suggesting either headgroup flexibility or phospholipid heterogeneity.

Quinone binding and electron transfer in the Ecbd dimer

The dimer interface of *Ecbd* is formed by CydX in conjunction with coordinated phosphatidylglycerol (PG) lipids (Fig. 3.2A,B). These PG lipids also interact with the CydA Q-loop via hydrogen bonding between $Arg298^{CydA}$ and the lipid carbonyl group. The homodimeric CydX–CydX interface is stabilized by a methionine–aromatic motif ($Met1^{CydX}$–$Trp2^{CydX}$) and a leucine zipper along the helical axis (Fig. 3.2B). Within the dimer, each *Ecbd* protomer contains three distinct quinone-binding pockets. The primary quinone binding site, located beneath the Q-loop, accommodates a well-resolved MK headgroup (Fig. 3.2C). This shallow, hydrophobic cavity is positioned 6.7 Å from the heme b_{558} iron center, enabling fast electron transfer. The MK isoprenoid tail is only partially resolved, indicating its flexibility during quinone binding and turnover. The MK headgroup is stabilized by π–π stacking with $Tyr243^{CydA}$ (4.5 Å) and hydrogen bonding with $Arg298^{CydA}$ (3.4 Å), both of which facilitate semiquinone stabilization and proton transfer during catalysis. This site is strongly implicated as the quinol oxidation center, as mutagenesis of either $Tyr243^{CydA}$ or $Arg298^{CydA}$ to alanine (Y243A, R298A) abolished enzymatic activity with both MK and UQ in *Ecbd* monomers, confirming its role as the principal quinol oxidation site (Fig. 3.2F). The arrangement of the three hemes in CydA follows a triangular topology, as previously described[83], with the MK-bound structure facilitating mapping of the full electron transfer route from the quinol oxidation site to the oxygen reduction center (Fig. 3.3A). Although no proton release pathway could be identified unambiguously, the protons released during quinol oxidation could transfer to the periplasm via the closely positioned $Asp239^{CydA}$ and $Glu240^{CydA}$ pair at the membrane interface, or transfer via a series of structured water molecules to the conserved $Lys252^{CydA}$ (Fig. S3.9). The associated electrons are transferred sequentially from this MK site via heme b_{558} to b_{595} (14.9 Å) and finally to heme *d* (11.2 Å), where molecular oxygen reduction occurs in two cycles of quinol oxidation (Fig. 3.3A).

A second quinone binding site is located at the CydA–CydX interface and contains a co-purified ubiquinone molecule (Fig. 3.2D).

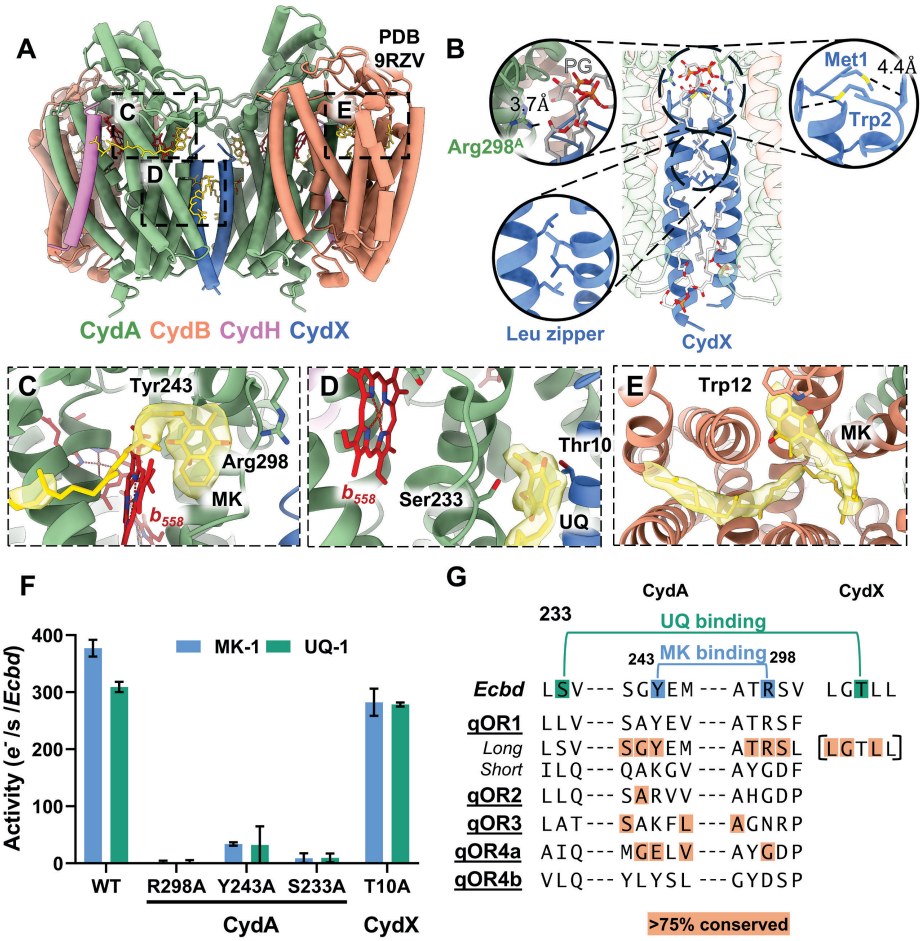


Fig. 3.2. The *Ecbd* dimer contains three distinct quinone binding sites per protomer (**A**) Overview of the *Ecbd* dimer and the quinone binding pockets. (**B**) The *Ecbd* dimer interface is formed CydX via Met-Trp interactions, and a leucine zipper. Additionally, a PG phospholipid forms a hydrogen bond with $Arg298^{CydA}$ further stabilizing the interface. (**C**) The Q binding site near heme b_{558}, showing a bound MK stabilized by $Tyr243^{CydA}$ and $Arg298^{CydA}$. (**D**) The UQ binding site wedged between subunit CydA and CydX. The UQ is stabilized by interactions with $Ser233^{CydA}$ and $Thr10^{CydX}$. (**E**) The quinone binding pocket in CydB with a bound MK, stabilized by π-π stacking with $Trp12^{CydB}$. The quinone headgroup is situated outside of electron transfer distance from the heme chain. (**F**) Oxidase activity of monomeric *Ecbd* WT and quinone binding site mutants (N=3). (**G**) Consensus sequence alignment of the qOR1-4 subfamilies as defined by Murali *et al.*[88] The qOR1 family was subdivided in long- and short-Q-loop cyt *bd* variants indicating conservation of $Y243^{CydA}$ and $R298^{CydA}$ in the long Q-loop family (extended sequence variation in table S3.2). The CydX subunit is only present in a subset of qOR1-long Q-loop family. The consensus sequence and conservation of CydX defined by Allen *et al.*[158]

This UQ is coordinated via a hydrogen-bonding network involving Ser233^{CydA} and Thr10^{CydX} of the same protomer. Positioned 14 Å from the heme b_{558} iron center and 13.2 Å from the primary MK site, this second site lies within electron transfer distance, with potential for both direct electron transfer and indirect electron transfer into the heme chain. However, although mutation of S233^{CydA} to alanine in the second quinone binding pocket (S233A) in CydA also fully inactivates *Ecbd*, mutation of T10^{CydX} to alanine (T10A) remains active (Fig. 3.2F). Although the activity of T10A^{CydX} strongly suggests the second quinone binding site is not a quinol oxidation site, we further investigate the abolished activity of the S233A^{CydA} mutant. Notably, analysis of the heme spectra reveals distinct alterations among the mutants. Both R298A^{CydA} and Y243A^{CydA} exhibit a partial decrease in heme *d* content or reduction, whereas in the S233A^{CydA} mutant heme *d* is completely absent. In addition, heme b_{558} in S233A is significantly shifted, indicating pronounced changes in the heme environment (Fig. S3.10). These observations suggest that S233^{CydA} plays a primarily structural role rather than a direct role in ubiquinol oxidation. Thus, while this site is capable of binding quinones tightly, retaining UQ even after incubation with excess MK, it likely does not function as a site for quinol oxidation.

A third quinone site, typically occupied by UQ in CydB[83,91], was found to contain MK in the MK-incubated structure (Fig. 3.2E). Although the density for this MK is less defined, indicating either heterogeneity or flexible binding, the headgroup appears repositioned near Trp12^{CydB}, in contrast to as isolated structures. Despite this rearrangement, the MK headgroup remains 30 Å from the heme *d* center and lacks nearby residues to stabilize a semiquinone, indicating a structural rather than catalytic role. Functional assays confirmed that quinone exchange at this site does not affect enzymatic activity, precluding any allosteric effects (Fig. S3.11).

Sequence alignment across the *bd*-type oxidases family revealed conservation of the Tyr243^{CydA} or Arg298^{CydA} residues exclusively within the qOR1-long Q-loop subfamily (Fig. 3.2G, Table S3.2), indicating an evolutionary divergence in quinol oxidation site architecture between short and long Q-loop variants.

Functional role of the quinone pool in Ecbd regulation

While *Ecbd* is active with both MK and UQ[159], we aimed to assess if the content of the quinone pool provides any regulation on *Ecbd* activity. However, classical solution-based assays fail to distinguish between MK and UQ when simultaneously present. To assess this putative allosteric regulation by the available quinone pool, we employed a tethered bilayer lipid membrane (tBLM) electrochemical system, which can distinguish UQ and MK based on their redox potentials. This system enables direct electron transfer from a gold electrode to membrane-embedded quinones (Fig. 3.3C)[160], and has previously been used to study a variety of respiratory enzymes[28,148,161]. To form the tBLM, *Ecbd* was reconstituted in liposomes doped with either MK-9 or UQ-10 as native-like substrates.

Formation of the tBLM was confirmed by a characteristic drop in surface capacitance[162]. Reduction of the quinone pool and subsequent quinol oxidation by *Ecbd* was monitored via cyclic voltammetry (CV). CV measurements revealed catalytic currents for both the UQ-10 and MK-9 *Ecbd* samples with identical onset potentials and similar catalytic currents, indicating that the co-purified UQ in the MK sample is redox-active and capable of supporting *Ecbd* turnover (Fig. 3.3D). Whether this activity originates directly from the CydA–CydX site or reflects quinone exchange at the primary quinol oxidation site remains to be determined. We conclude that *Ecbd* is promiscuous regarding the quinol pool and not allosterically regulate by either UQ or MK.

Proton and oxygen delivery to the oxygen reduction center

Following the reduction of heme *d*, molecular oxygen and protons need to be guided towards the oxygen reduction site to complete the catalytic cycle. Using Mole 2.5[163] we identified two distinct channels converging at the heme *d* site, previously deemed the proton and oxygen channels (Fig. 3.3B)[83]. The oxygen channel (O-channel) originates between helices 1 and 9 of CydB and runs parallel to the membrane. The channel is lined with hydrophobic residues to facilitate the preferential entry of molecular oxygen. Near heme *d*, the

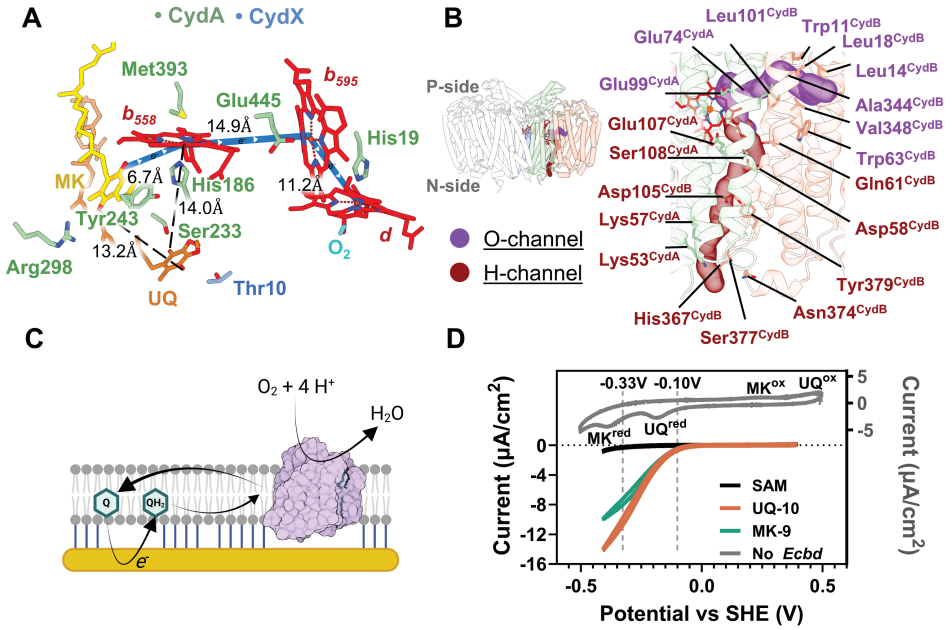


Fig. 3.3. The electron transfer, proton, and oxygen pathways (**A**) Proposed electron transfer routes from the MK (yellow) depicted in dark blue. Distances from UQ (orange) to MK and heme b_{558} are indicated. (**B**) Residues lining of the O- and H-channel leading towards the heme *d* oxygen reduction center. (**C**) Overview of the tBLM electrochemical system, where the quinone pool is directly reduced at the gold electrode to initiate *Ecbd* turnover. (**D**) Cyclic voltammograms of the tBLM system. Inset in grey shows a model membrane containing both MK (1 mol%) and UQ (1 mol%) without *Ecbd* (100 mV/s scan rate). The reduction and oxidation peaks of UQ and MK are indicated. The SAM negative control (black), *Ecbd* tBLMs containing only UQ-10 (Orange), or MK-9 (Green) (10 mV/s scan rate) showing the same onset potential at the reduction of UQ.

channel is terminated by two glutamate residues providing hydrogen bonding during oxygen reduction.

The H-channel originates at the CydA-CydB interface and extends perpendicularly from the cytoplasmic side toward heme *d*, and is lined with titratable residues forming a putative proton wire. Our predictions using PROPKA of residue pKa suggest proton transfer involving $Lys53^{CydA}$ (pKa 9.01), $Lys57^{CydA}$ (pKa 7.45), $Asp105^{CydB}$ (pKa 4.53), $Asp58^{CydB}$ (pKa 8.14), $Glu107^{CydA}$ (pKa 9.47), and $Glu74^{CydA}$ (pKa 11.07). The high pKa of $Lys53^{CydA}$ allows for fast proton extraction from the cytoplasm to increase turnover rates. Among the channel

residues, Asp105^{CydB} emerges as the most acidic and has been previously implicated as critical in proton transfer[164]. Notably, Glu107^{CydA}, positioned 7.8 Å from the heme *d* iron center, exhibits a pKa consistent with the proposed terminal proton donor identified by Janczak *et al.*[164] and is highly conserved across CydA homologues (>90% sequence conservation)[88]. These findings support a model in which Lys53^{CydA} initially extracts protons from the cytoplasm, after which Glu107^{CydA} serves as the primary proton donor for oxygen reduction, completing the proton delivery pathway.

Closing of the Q-loop lid completes the quinol oxidation site and enhances catalytic efficiency

Despite exposure to high concentrations of MK, no density is observed near the Q-loop in monomeric *Ecbd*, indicating persistent conformational flexibility. This precludes reliable modeling of residues Glu239–Gly306^{CydA} in the *Ecbd* monomer. Structural comparison between monomeric and dimeric *Ecbd* revealed a rotation of Trp2^{CydX} upon dimerization, facilitating hydrogen bonding with Asp239^{CydA} (Fig. 3.4A,B). This interaction anchors the Q-loop segment spanning Asp239–Asp247^{CydA}, positioning Tyr243^{CydA} optimally for quinol capture. Together, this suggests that the dimeric state is more conducive to MK binding and, hence, MK oxidation.

Ecbd monomers and dimers were separated using gel filtration to probe the activity of the individual states. After isolation in LMNG, the monomeric and dimeric *Ecbd* remained in their oligomeric state as shown by SEC-MALS. This indicates that after isolation there is no re-equilibration between monomer and dimer, even after incubation with various lipids or quinones, enabling kinetic evaluation of the distinct monomeric and dimeric *Ecbd* (Fig. S3.12). Catalytic activity was assessed using a coupled assay in which quinones were reduced by an excess of NADH dehydrogenase[159]. The oxygen consumption rate was determined using an oxygraph and recalculated into *Ecbd* activity at 4 electrons per oxygen reduced. The observed structural stabilization in the *Ecbd* dimer correlates with a twofold increase in catalytic turnover rate relative to the monomer, without a substantial change in substrate K_m (Fig. 3.4C).

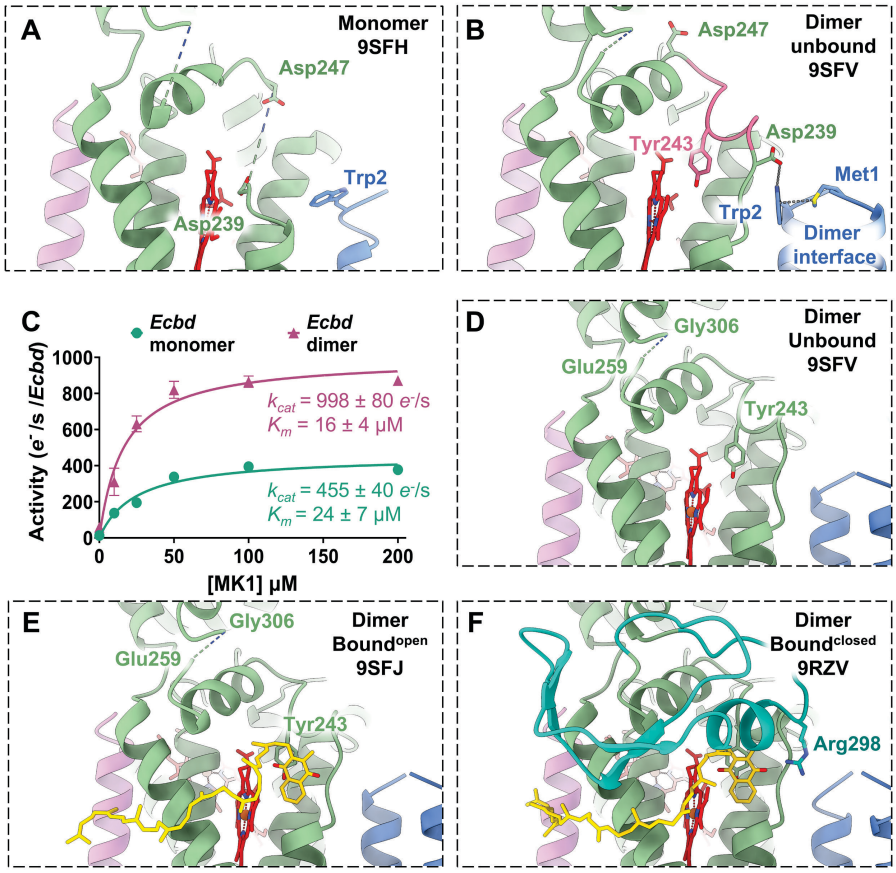


Fig. 3.4. Q-loop stabilization increases the turnover rate in the *Ecbd* dimer (**A**) Selected view of the quinone binding pocket in the *Ecbd* monomer (**B**) and in the *Ecbd* dimer. The pink stretch is stabilized by hydrogen bonding between Asp239^{CydA} and Trp2^{CydX}, positioning Tyr243^{CydA} for quinol capture. (**C**) Michaelis Menten kinetics of the *Ecbd* monomer and dimer (N=3). (**D**) unbound *Ecbd* dimer. (**E**) *Ecbd* dimer in the MK bound^{open} state showing initial interaction with the quinone. (**F**) *Ecbd* dimer in the bound^{closed} state showing closing of the Q-loop lid. CydA is represented in green, with the Q-loop lid in cyan. CydH is represented in violet, with CydX in blue.

This behavior could be explained if quinol dissociation is much faster than quinol oxidation in both monomer and dimer, while quinol oxidation proceeds slower in the monomer. Under this assumption, *Km* would approximate the quinol dissociation constant (K_d), which would seem to be unchanged in dimer versus monomer. Alternatively, if quinol dissociation occurs on slower or

similar timescale as its oxidation, K_m could remain unchanged if both the substrate binding rate and catalytic turn-over are slower in the monomer. As transient Q-loop remodeling is required in the monomer to position Y243^{CydA} for quinol capture, it is possible if not likely that this conformational transition is rate-limiting in the monomer. In contrast, the dimeric enzyme maintains a partially-formed, catalytically competent quinol oxidation site. We propose that this results in a higher rate of substrate binding and catalysis for the *Ecbd* dimer, which together improve catalytic turnover without substantially changing K_m. We cannot exclude that the catalytic rate of the dimer might be limited by product release. While this would explain why quinone binding is only observed in the dimer, the Michaelis-Menten kinetics cannot unambiguously determine the rate limiting step.

Although the Asp239–Asp247^{CydA} segment is stabilized in the dimer, the remainder of the Q-loop remains disordered in the unbound state (I) (Fig. 3.4D). This precludes modelling of the amino acid stretch between Glu259^{CydA} and Gly306^{CydA}, hereafter referred to as the Q-loop lid. This flexible region remains unstructured even after initial MK engagement by Tyr243^{CydA} (MK bound^{open}, II) (Fig. 3.4E). Only in this MK bound state can the Q-loop lid undergo a structural rearrangement to stabilize the fold, enabling confident modelling of side chains and revealing the complete quinol oxidation site architecture (MK bound^{closed}, III). The Q-loop lid wraps around the quinone binding site before looping back onto the main body of CydA, mirroring the fold found in *Ecbd-II* and *M. tuberculosis* cyt *bd* (Fig. S3.13)[82,87]. The rearrangement of the Q-loop lid allows for hydrogen bonding between Arg298^{CydA} and the quinone headgroup, completing the quinol oxidation site for turnover (Fig. 3.4F).

Inhibition by Aurachin D triggers active site refolding

AurD, a MK analog derived from *Stigmatella aurantiaca*, is a potent and specific inhibitor of cyt *bd* oxidases[100]. To elucidate its mechanism of action, we resolved cryo-EM structures of both monomeric and dimeric *Ecbd* in the presence of AurD. While no density for AurD was observed in the monomer, the

dimeric structure revealed clear binding near the quinol oxidation site (inhibitor bound, IV) which allows for unambiguous modeling of the AurD binding pose (Fig. 3.5A). Surprisingly, AurD does not bind in the same pocket as MK, but induces a remarkable conformational change in helix 6, converting it from a loop into an α-helix. This conformational change closes the quinone binding pocket, effectively blocking substrate access. Close examination of the refolding process indicates that Asp239^{CydA} forms a hydrogen bond to the AurD amine group and hereby pulls the loop inwards to stabilize the helical conformation (Fig. 3.5B). The AurD headgroup is further stabilized by hydrophobic interactions with Gly242^{CydA}, Tyr243^{CydA}, Leu253^{CydA}, Glu257^{CydA}, Phe269^{CydA}, Ile295^{CydA}, Ala296^{CydA}, Phe298^{CydA}, Phe390^{CydA}, Arg391^{CydA}, Val394^{CydA}, Ala395^{CydA}, and heme b_{558} (Fig. 3.5C). These hydrophobic interactions in the AurD binding pocket are conserved across the *bd* oxidase families, while Asp239^{CydA} is mainly conserved in the qOR1-long Q-loop family (Fig. 3.5D, Table S3). Interestingly, AurD binding occurs deeper into the binding pocket compared to the binding in *Ecbd*-II[87] (Fig. S3.14).

To confirm Asp239^{CydA} as the main effector residue for inhibition with AurD we performed mutagenesis (D239A^{CydA}). Although Asp239^{CydA} lies outside the quinol oxidation site in the MK-bound state, its mutation to alanine abolishes enzymatic activity, resulting in the inability to support bacterial growth in the MB43 strain lacking all terminal oxidases in the genome (Fig. 3.5E, Fig. S3.15), consistent with prior reports[165]. We postulate that inactivity of the *Ecbd* D239A^{CydA} mutant results from the impairment to form the hydrogen bond with Trp2^{CydX} (Fig. 3.3B), effectively closing the MK binding pocket as seen in the AurD bound state. In contrast, substitution with glycine partly preserves activity while significantly reducing AurD sensitivity (Fig. 3.5E,F), confirming Asp239^{CydA} as a key determinant of inhibitor binding and efficacy, as seen in *Ecbd*-II[87].

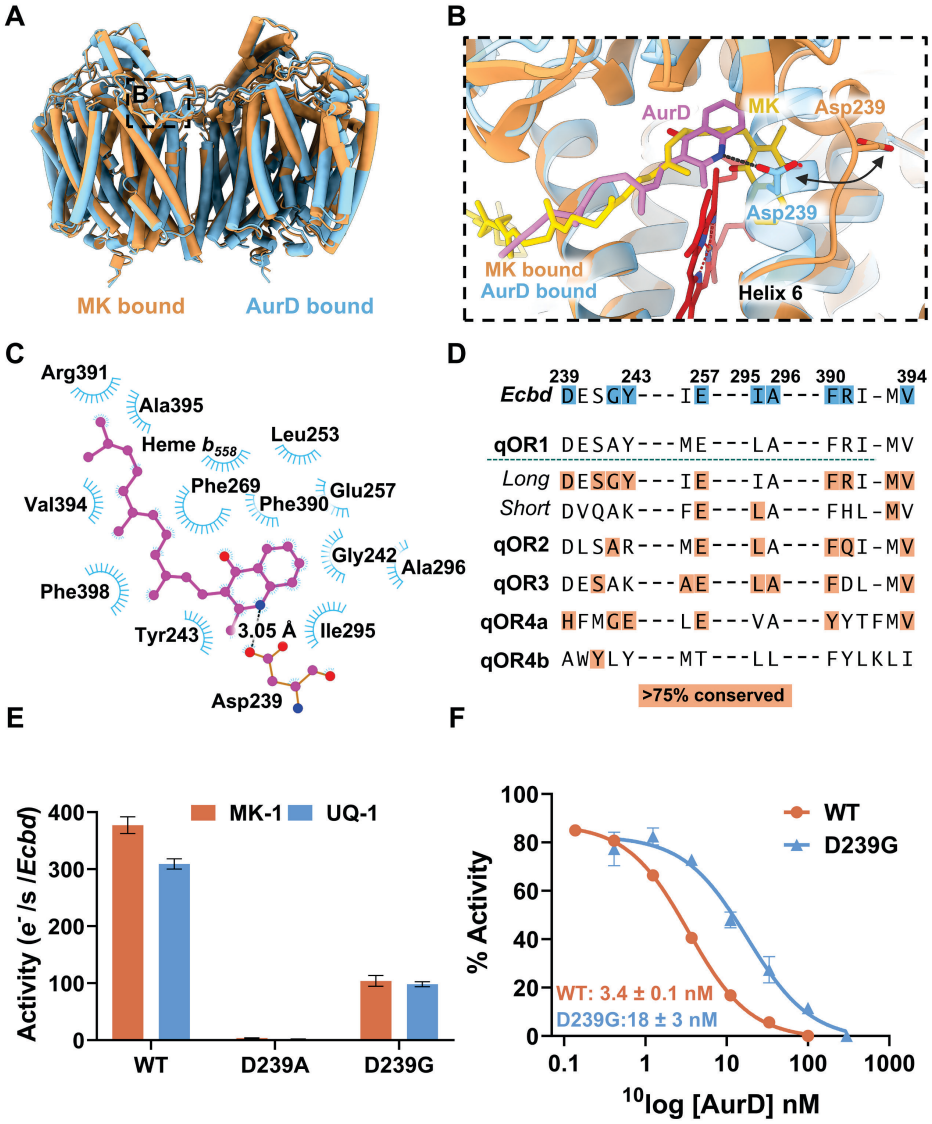


Fig. 3.5. Inhibitory mechanism of Aurachin D. (**A**) Overview of the *Ecbd* dimer in the MK and AurD bound state. (**B**) Refolding of the *Ecbd* active site by AurD by the attraction of $Asp239^{CydA}$. (**C**) Two dimensional representations of the interactions in the AurD binding pocket. (**D**) Conservation of the AurD binding pocket residues. (extended sequence variation in table S3.3) (**E**) Activity of the monomeric *Ecbd* WT and $D239A^{CydA}$ and $D239G^{CydA}$ mutants (N=3). (**F**) IC_{50} of AurD against the monomeric *Ecbd* WT and $D239G^{CydA}$ mutant (N=3), P<0.001.

Discussion

The structural and mechanistic insights presented here establish a comprehensive framework for understanding quinone turnover, electron transfer, and inhibition in *bd*-type oxidases. Prior structural studies of cyt *bd* oxidases have predominantly captured the enzyme in a monomeric state, with no resolved structures of the quinol oxidation site. A notable exception is the dimeric structure of *E. coli* cyt *bd*-II bound to AurD, resolved in amphipols at 3.0 Å resolution[87]. However, the physiological relevance of this dimeric state remained uncertain, as it was speculated to be an artifact of amphipol reconstitution. Using a cryo-EM approach we were able to resolve the dimeric state of *Ecbd* in detergent and nanodiscs, and show it as a native state *in vivo* by SMALP isolation and the presence of native *E. coli* lipids at the dimer interface. The CydX dimer interface is well conserved, indicating common dimerization of cyt *bd* in the species containing the CydX subunit[158]. Interestingly, CydX is solely found within a sub-population of the qOR1-long Q-loop family, showing further divergence within cyt *bd* oxidases[158]. Similar, but not homologous, single-helical subunits are found in short Q-loop *bd* oxidases, such as CydS in *G. thermodenitrificans* cyt *bd* [81]. CydS, however, does not seem to facilitate dimer formation in AlphaFold prediction (Fig. S3.14). In addition, CydS has a profoundly different sequence than CydX, indicating a role in stabilization rather than dimerization.

Functionally, the dimeric form of *Ecbd* exhibits significantly enhanced catalytic activity compared to the monomer, suggesting that dimerization is physiologically important for its function. In the monomeric state, the Q-loop remains disordered despite quinone availability, suggesting that formation of the quinol oxidation site is transient and rate-limiting. This is further supported by previous studies showing that the deletion of the dimer-forming subunit CydX compromises *Ecbd* expression, stability, and activity[92,166]. We hypothesize that dimerization could serve as a regulatory mechanism, enabling *Ecbd* to become catalytically enhanced under microaerobic conditions when it is upregulated to assist the more energetically efficient

cytochrome bo_3. This dynamic switch may allow *E. coli* to balance respiratory efficiency with adaptability to stress.

The *Ecbd* dimer shows quinone (product) binding in a shallow peripheral pocket that stabilizes only the headgroup, consistent with rapid substrate exchange from the quinone pool. This primary quinol oxidation site, located beneath the Q-loop lid near heme b_{558}, is stabilized by CydA residues $Tyr243^{CydA}$ and $Arg298^{CydA}$, both uniquely conserved in qOR1-long Q-loop *bd* oxidases (Fig. 3.2G). This conservation underscores a mechanistic divergence from the other subfamilies. Moreover, $Tyr243^{CydA}$ and $Arg298^{CydA}$ are distinctly different from the previously indicated quinol oxidation site residues, $Lys252^{CydA}$, $Glu257^{CydA}$, and $Glu280^{CydA}$[113]. These latter residues stabilize the Q-loop in the MK bound form by forming hydrogen bonding with the main body of CydA, which could explain the drop in activity upon mutation[113].

The Q-loop undergoes a disorder-to-order transition upon quinone binding, completing the quinol oxidation site and enabling catalysis. This large structural rearrangement during the catalytic cycle represents substantial energetic investments to form the catalytically active state. Such large structural rearrangement during catalysis has previously been indicated to prevent irreversible binding of the substrate while presenting a binding pocket highly optimized for the transition state[167]. This means that the closed Q-loop state could represent an intermediate specifically stabilized by the semi-quinone. The binding energy associated with this state will release upon quinone formation, expelling the quinone from the active site to improve turnover rates. This mechanistic adaptation might allow cyt *bd* to maintain high catalytic activity and low K_m, necessary to uphold membrane potential despite displacing less protons than cytochrome bo_3 or other pumping terminal oxidases[167].

In addition to the primary site, we identified a secondary ubiquinone-binding pocket at the CydA–CydX interface. This site is specific for UQ and mutagenesis suggests it contributes to structural stabilization of the dimer rather than direct catalysis. Additionally, neither the evolution of the long Q-loop, nor the addition of the CydX subunit seem critical for ubiquinol turnover, as neither the

long Q-loop nor a CydX subunit is found in *Pseudomonas aeruginosa* which can utilize ubiquinol[168] (Fig. S3.14). We hypothesize that oxidation of ubiquinol substrates in *Ecbd* is catalyzed at the same menaquinol oxidation site identified in this study. Furthermore, we did not observe any substrate preference or allosteric modulation in the presence of both UQ and MK (Fig. 3.3D).

A particularly notable finding is the dual role of $Asp239^{CydA}$. This residue is essential for both quinol oxidation site stabilization and inhibition by AurD. Despite the structural similarity between MK and AurD, AurD binding induces a remarkable refolding of helix 6 into an α-helix, preventing substrate access. Interestingly, this α-helical conformation mirrors that observed in all solved structures of short Q-loop *bd* oxidases (Fig. S3.16)[80,82,84]. Despite the sequence and structural conservation of the binding pocket in *M. tuberculosis* cyt *bd*, no densities have been observed for AurD in the presence of vast molar excesses[82]. To probe a similar binding poses of AurD in short Q-loop *bd* oxidases, we performed docking in the *M. tuberculosis* cyt *bd* Q-loop. Despite the conservation of the pocket, no similar binding pose was observed (Fig. S3.17). This raises the possibility that short Q-loop *bd* oxidases undergo structural rearrangement of the Q-loop lid upon turnover, as shown here for *Ecbd*. This conformational change might be present only transiently, or require additional binding partners, prohibiting direct structural interrogation. Alternatively, we cannot exclude that short Q-loop *bd* oxidases have evolved a fundamentally distinct catalytic mechanism, and therefore inhibition with AurD, explaining why no quinone or AurD binding in these enzymes has been observed[80–82,84].

The series of cryo-EM structures presented here enables us to propose a global overview of the entire quinol oxidation mechanism (Fig. 3.6). Even though our quinone bound structures represent the product rather than the substrate, we postulate that the minor difference in substrate (quinol) and product (quinone), do not result in major structural changes and therefore represent either state. We cannot exclude, however, that the equilibria between the different states change depending on the binding of either quinone or quinol. The catalytic cycle starts in the unbound state, in which the Q-loop remains flexible, and $Tyr243^{CydA}$ is positioned for quinol capture (Fig. 3.6A). After quinol

binding (Fig. 3.6B), the Q-loop undergoes a conformational transition that closes the lid and completes the quinol oxidation site by forming a hydrogen bond between Arg298^{cydA} and the quinol head (Fig. 3.6C). Proton-coupled electron transfer proceeds with electrons relayed through the heme chain to the oxygen reduction site at heme *d* (Fig. 3.6D), after which the Q-loop opens and the quinone is released (Fig. 3.6E). A second sequence of quinol oxidation occurs, during which O_2 is fully reduced to two H_2O, completing the *Ecbd* turnover cycle.

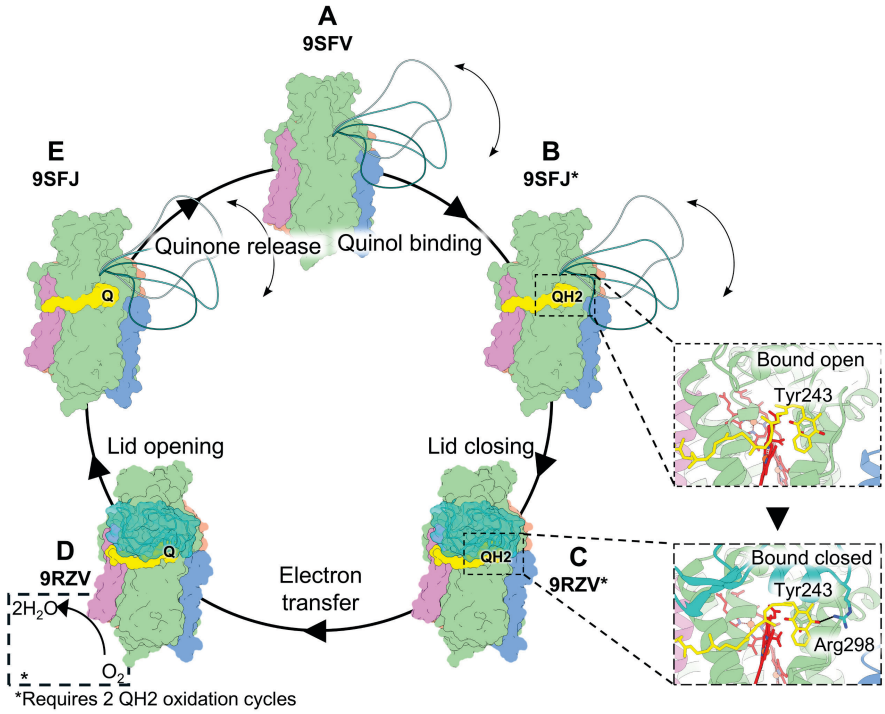


Fig. 3.6. Schematic overview of the proposed turnover mechanism of *Ecbd*. (A-D) Overall schematic view of *Ecbd* turnover. States with an asterix are presumed to be structurally the same in the quinol and quinone bound states. (**A**) The unbound *Ecbd* dimer has a flexible Q-loop lid and sits ready for quinol binding. (**B**) The *Ecbd* dimer undergoes quinol binding. (**C**) From the quinol bound state (**C1**), the Q-loop lid closes, finishing the formation of the quinol oxidation site by coordinating Arg298^{CydA} to the quinol head (**C2**). (**D**) Electron transfer occurs via the heme chain onto molecular oxygen. (**E**) The Q-loop lid opens to release the quinone and start another catalytic cycle.

Together, these insights provide a detailed molecular blueprint of *Ecbd* function and establish a foundation for rational drug design targeting *bd*-type oxidases. Given the essential role of cyt *bd* in the survival of several clinically relevant pathogens, these findings have broad implications for the development of next-generation antibiotics.

Experimental procedures

Structure guided mutagenesis

Structure guided *Ecbd* mutagenesis was performed on the pET17b-CydABX-linkerstreptag[92] plasmid using Whole Plasmid Synthesis or Gibson assembly (See Table S4 for primers). Mutants were confirmed using Sanger sequencing.

Ecbd purification

The expression of *E. coli* cytochrome *bd*-I (*Ecbd*) was performed as stated previously[90]. Briefly, MB43 cells[144,145] transformed with pET17b-CydABX-linkerstreptag or MB43ΔCydA[90] transformed with the mutant plasmids were grown overnight in LB with 100 µg/mL ampicillin (250 RPM, 37°C). The WT culture was diluted to OD ~0.1 and grown to OD ~0.4 before induction with 0.45 mM IPTG. At OD 2.0 the cells were harvested by centrifugation (6371 rcf, 20 min, 4°C) and resuspended in 50 mM MOPS, pH 7.4, 100 mM NaCl, cOmplete™ EDTA-free Protease Inhibitor (ROCHE), at 5 mL per 1 gram of wet cells. The *Ecbd* mutants were expressed overnight and otherwise followed the same procedure. The cells were lysed by a passing through a Stansted pressure cell homogeniser (270 MPa). Cell debris were pelleted by centrifugation (10.000 rcf, 20 min, 4°C). Crude membranes were isolated by ultra-centrifugation (200.000 rcf, 1h, 4°C) followed by resuspension in 50 mM MOPS, 100 mM NaCl, pH 7.4 (10 mg/mL total protein). Solubilization of the *Ecbd* was performed by incubation with 0.5% Lauryl maltose neopentyl glycol (LMNG) for 1 hour at 4°C with gentle mixing. Insoluble material was pelleted by ultra-centrifugation (200.000 rcf, 30 min, 4°C) followed by application of the soluble fraction to a StrepTrap HP column (Cytiva) at 2 mL/min. The column was washed with 50 mM sodium

phosphate, 300 mM NaCl, 0.005% LMNG, pH 8.0 to remove unbound proteins. *Ecbd* elution was performed by addition of 50 mM sodium phosphate, 300 mM NaCl, 2.5 mM desthiobiotin, 0.005% LMNG, pH 8.0, after which purity was confirmed by SDS-page. If needed, *Ecbd* dimers and monomers were separated using size exclusion chromatography (SEC) on a Superdex increase 200 10/300 column (Cytiva) at 0.5 mL/min (50 mM sodium phosphate, 300 mM NaCl, 0.005% LMNG, pH 8.0). The defined fractions were pooled, concentrated, and stored at -80°C until further use.

NDH2 purification

NDH2 was required to reduce the quinone pool in order to measure *Ecbd* activity. Expression and purification of NDH2 were performed as previously described[159]. Briefly, C41 (DE3) cells, transformed with pET28-NDH-2_NtermHis, were grown overnight LB Kanamycin (250 RPM, 37°C). The culture was diluted 20-fold and grown to ~OD 0.5 before induction with 0.25 mM IPTG. NDH2 expression was maintained for 4 hours at 37°C before harvesting by centrifugation (6371 rcf, 20 min, 4°C). The cells were resuspended in a 5 mL of 50 mM Tris-HCl, 5 mM $MgCl_2$, pH 8.0 per 1 gram of cells, and disrupted by passing through a Stansted pressure cell homogeniser (270 MPa). Cell debris were pelleted by centrifugation (10.000 rcf, 20 min, 4°C) before harvesting of the crude membranes by ultra-centrifugation (200.000 rcf, 1h, 4°C). The membranes were resuspended in Tris-HCl, 150 mM NaCl, 20 mM Imidazole (10 mg/mL total protein). NDH2 was extracted by treatment with 1% DDM for 1 hour at 4°C with gentle mixing. The remaining insoluble material were removed by ultra-centrifugation (200.000 rcf, 30min, 4°C) before application of the soluble fraction on a HiTrap Nickel NTA column (Cytiva). The unbound proteins were washed from the column with 50 mM Tris-HCl pH 8.0, 150 mM NaCl, 20 mM Imidazole, 0.02% DDM. NDH2 was eluted by addition of 30% elution buffer (50 mM Tris-HCl, 150 mM NaCl, 500 mM Imidazole, 0.02% DDM). Final purification was achieved by gel filtration on a Superdex increase 200 10/300 column (Cytiva) at 0.5 mL/min (50 mM Tris-HCl, 500 mM NaCl, 5% glycerol, 0.02% DDM). Pure NDH2 fractions were pooled, concentrated, and stored at -80°C until further use.

MSP1D1 expression and purification

MSP1D1 expression was performed as described before[169]. Briefly, BL21(DE3) pLysS transformed with pET28a containing the MSP1D1 gene[169] were grown in terrific broth at 37°C, 200 RPM until OD ~2.0. The cultures were cooled to 30°C before induction with 1 mM IPTG. The cells were induced for 5 hours, followed by cell harvesting (10.000 rcf, 20 min, 4°C). The cells were resuspended in 50 mM Tris-HCl (pH 8.0), 300 mM NaCl, 1% Triton X-100. The cells were lysed by a single pass through a Stansted pressure cell homogeniser (270 MPa). Debris and membrane fractions were pelleted by ultra-centrifugation (200.000 rcf, 1h, 4°C). The supernatant was applied to a HisTrap (Cytiva) column followed by extensive washing with buffer containing 1% (w/v) Triton X-100 and 50 mM Na-cholate. Finally, the MSP1D1 was eluted using 50 mM Tris, 300 mM NaCl, 300 mM Imidazole. The MSP1D1 peak fractions were concentrated and further purified on a HiLoad 16/100 75 pg column (Cytiva) using 50 mM Tris-HCl, pH7.5, 200 mM NaCl. The peak fractions were concentrated to 10 mg/mL and stored at -80°C until further use.

Ecbd reconstitution in nanodiscs

Ecbd nanodiscs were assembled as described previously with slight modifications[83]. Briefly, the POPC:MK-9 mixture was dissolved in 20 mM HEPES (pH 7.4), 150 mM NaCl 100 mM Na-cholate by sonication. Following, MSP1D1, POPC, MK-9 and *Ecbd* were mixed at the molar ratio of 20:760:40:1 and incubated for 1h on ice. The detergent was removed by the stepwise addition of 5% w/v SM-2 biobeads every two hours, totaling 15% w/v before overnight incubation at 4°C while mixing. The biobeads were removed by filtration before application of the nanodisc mixture on a Superdex increase 200 10/300 column (Cytiva) at 0.5 mL/min (20 mM HEPES, 150 mM NaCl, pH 7.4). *Ecbd* nanodisc peak fractions were concentrated and used for further analysis and grid preparation.

SEC-MALS analysis

The *Ecbd* in detergent or nanodiscs were characterized using a SEC-MALS system comprised of a miniDAWN® TREOS®, Optilab differential refractometer (Wyatt technology) and 1260 Infinity II multiple wavelength absorbance detector (Agilent). The nanodisc composition was determined using the protein conjugate method in Astra software (Version 8) after defining the $dn/dc_{protein}$, dn/dc_{lipids} and ε_{417nm}, protein. *Ecbd* monomer and dimer equilibria were determined after incubation with lipids, quinones or Aurachin D.

Ecbd oxygen consumption

Oxygen consumption of *Ecbd* was measured on an oxygraph (Hansatech Ltd.) system at 20°C[159]. The quinone (MK-1 or UQ-1) was added to the reaction chamber at the indicated concentration in 50 mM MOPS, 150 mM NaCl, (0.005 LMNG if needed) pH 7.0. The enzymatic quinone reduction with *C. thermarum* NDH-2 (30 nM) was initiated by the addition of 1 mM NADH, followed by the determination of the quinone autooxidation (background). Oxygen consumption was initiated by the addition of *Ecbd* (4 nM). The enzyme activity was measured by subtraction of the quinone autooxidation rate from the initial slope after *Ecbd* addition. In case of IC_{50} determination, the desired amount of AurD was added after *Ecbd* addition. The slope after AurD addition was divided by the slope before AurD addition to determine the inhibition rate. For direct kinetic comparison of *Ecbd* with its mutants, monomeric *Ecbd* was used.

Ecbd reconstitution in proteoliposomes for electrochemistry

Lipids dissolved in chloroform were purchased from Avanti Polar Lipids. A lipid mixture of POPE:POPG:CA 60:30:10, enriched with the 1 mol% of ubiquinone-10 (UQ-10) (Sigma) or menaquinone-9 (MK-9) (Caymen chemical), was dried under a stream of nitrogen followed by overnight incubation under vacuum. The lipids were rehydrated to a final concentration of 10 mg/mL (20 mM MOPS, 30 mM

Na_2SO_4, 100 mM KCl, pH 7.4) and extruded to 200 nm using an Avanti extruder. *Ecbd* reconstitution was performed as previously described[148]. LMNG solubilized *Ecbd* was added to the liposome solution at 1 w/w% protein/lipids and mixed for 30 min by inversion at RT. Insoluble materials were removed by centrifugation in an Eppendorf tabletop centrifuge (14100 rcf, 5 min). The reconstituted *Ecbd* concentration was determined by re-dissolving a sample in 2% octyl-β-glucoside, followed by quantification of the Soret band (ε_{417} 230 $mM^{-1}\,cm^{-1}$).

Electrode preparation and electrochemistry in a tBLM system

Template-stripped gold (TSG) electrodes were produced in-house by evaporating a 150 nm thick 99.99% pure Au layer (Thessco) on a cleaned atomically smooth silicon wafer using a Plassys MEB600SL E-beam Evaporator operating at 10^{-8} mbar. The gold deposition was monitored using a piezoelectric quartz crystal at 6.0 MHz. Glass slides (1.2 cm^2) were glued onto the gold layer with Epo-Tek 377 two-component glue and heated to 120°C for 2 hours for curing. Functionalization of the TSG electrodes with a self-assembled monolayer (SAM) was achieved by overnight incubation of freshly stripped electrodes in a mixture of 0.11 mM EO3-cholesteryl[170], 0.89 mM 6-mercaptahexanol (Sigma) dissolved in 2-propanol. Prior to measurement, the functionalized TSG electrodes were washed with 2-propanol and thoroughly dried under a stream of nitrogen. The TSG electrodes were placed into a custom polyether ether ketone (PEEK) sample holder with a Viton® O-ring seal (A = 0.29 cm^2). The sample holder was placed into a custom electrochemical cell and submerged in the electrolyte solution (20 mM MOPS, 30 mM Na_2SO_4, pH 7.4). The electrochemical setup was completed by the addition of a Pt counter electrode, a saturated double junction Ag/AgCl (sat. KCl) reference electrode (Radiometer analytical) and placing it in a steel Faraday cage. All potentials are given versus standard hydrogen electrode (SHE) using 0.199 mV vs SHE for the Ag/AgCl reference electrode. The electrochemical measurement was performed using an Autolab (Eco Chemie) electrochemical analyzer equipped

with a PGSTAT30 potentiostat and a FRA2 frequency analyzer. Impedance spectroscopy (EIS) was used to confirm that the SAM consisted of ~50% EO3-cholesterol, as described previously[171]. The electrolyte solution was purged with 95% Ar, 5% O_2 to remove most oxygen. Cyclic voltammograms were taken at 10 mV/s by holding the potential at 0.4 V vs SHE for 5 seconds and scanning between 0.4 and -0.4 V vs SHE. Background cyclic voltammograms of the SAM were taken before the addition of the tethered bilayer lipid membrane (tBLM) system to the electrode. The tBLM was created by the addition of 10 mM $CaCl_2$ and *Ecbd* proteoliposomes with 1 w/w% quinone (UQ-10 or MK-9) to a concentration of 0.5 mg/mL. The formation of the tBLM was followed by impedance spectroscopy and deemed finished once the signal stabilized (~1 hour). The catalytic activity of *Ecbd* was measured using cyclic voltammetry.

Cryo-EM sample preparation and data collection

Quantifoil UltrAUfoil R1.2/1.3 grids (mesh 300) were glow discharged with a PELCO easiGlow device at 15 mA for 90s on the foil side and 60 seconds on the other. *Ecbd* nanodiscs or in LMNG micelles (4 µL, 1.5 mg/ml), supplemented 100 with µM AurD if needed, were applied to the grid, followed by blotting at 4°C, 100% humidity, 20 blot force for 4 seconds using a Vitrobot IV device (Thermo Fisher) immediately before plunge freezing in liquid ethane. Blot time for *Ecbd* in LMNG was increased to 6 seconds.

Grids were either imaged on a Titan Krios G1 (ThermoFisher Scientific) operating at 300 kV, equipped with a Gatan K3 detector and BioQuantum energy filter with a slit width of 20 eV, or a Titan Glacios (ThermoFisher Scientific) operating at 200 kV with a Falcon 4i detector and selectris energy filter with a slit width of 20 eV. Movies were gathered in electron counting mode using aberration-free image-shift (AFIS) in EPU (ThermoFisher Scientific). A total dose of 100 e/Å^2 with 100 frames, at 105,000× magnification with a calibrated pixel size of 0.836 Å (Krios), or a magnification of 130,000× with a calibrated pixel size of 0.880 Å (Glacios), at and a defocus range of -0.8 to -2.0 µm.

Cryo-EM data analysis

Data processing was performed in CryoSPARC. Image preprocessing was performed in CryoSPARC live[150] using Patch Motion Correction and Patch CTF estimation. The processed micrographs were exported to CryoSPARC for further processing. Initial particle picking was performed with blob picking, followed by template generation for both the monomer and dimer particles. Template particle picking was performed for the monomer and dimer particles followed by multiple rounds of 2D classification to remove junk particles. Three volume unsupervised *ab-initio* model generation was performed to generate initial and bait volumes for further particle cleanup. Multiple rounds of heterogenous refinement were performed until the best class with clean particles became consistent. This clean particle stack was moved to Non-uniform refinement[151] for local CTF refinements and higher order aberration fitting. The movies were reprocessed in patch-based motion correction to remove the last 50 frames to account for accumulated beam damage. The particles were subjected to reference based motion correction[172], followed by another round of Non uniform refinement before assessment of heterogeneity using 3D classification. Dimer particles in the unbound dataset were split into the unbound and a bound-open class. The local resolution was improved using local refinement masking a single *Ecbd* protomer in the *Ecbd* dimer.

Model building and analysis

Model building was started from pdb 6RKO for the *Ecbd* monomer and an AlphaFold[173] prediction for the dimer. Model building was performed in Coot software[174] (version 0.9.8.1) followed by real space refinement in Phenix[175] (version 1.21.1-5286). Models and their corresponding maps were assessed and analyzed in ChimeraX[176] (version 1.7.1). Interior cavities and tunnels were analyzed using MOLEonline[163] (5 probe, 1 interior threshold, 5 origin radius, 8 surface over radius, 1.1 bottleneck radius, 3 bottleneck tolerance). The pKa of the titratable residues along the proton channel were estimated using PROPKA. Ligand binding pockets were visualized using LigPlot+[177].

Sequence alignment

For analysis of conserved residues, the multiple sequence alignment of Muralli *et al.*[88] was utilized, with additional division of qOR1 into the long and short Q-loop subfamilies. The sequence alignment was visualized using jalview, and reported as the consensus sequence with residues colored according to conservation >75%. The consensus sequence for CydX was taken from Allen *et al.*[158].

UV-Vis spectroscopy

Heme reduction in the *Ecbd* WT and mutants was analysed using an oxidized minus reduced spectrum. *Ecbd* was oxidized with 0.25 mM hexacyanoferrate in 50 mM NaPi, 300 mM NaCl, 0.005% LMNG, pH 8 and reduced by adding a few grains of sodium dithionite. Specific heme reduction was found by substracting the oxidized from the reduced spectrum. The spectra were normalized to the Soret band at 417 nm of the respective oxidized spectra.

Supplementary information

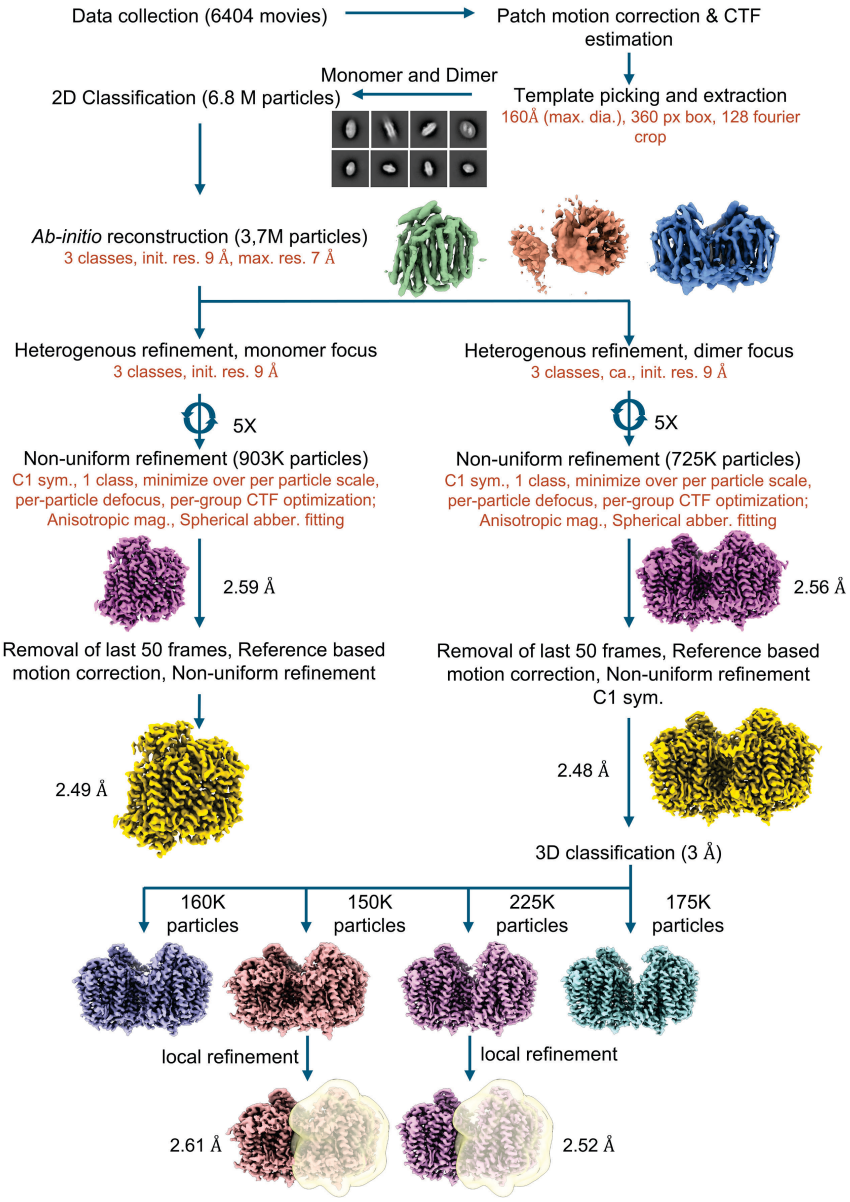


Figure S3.1: Cryo EM processing of the *Ecbd* unbound and bound^{open} structures (9SE4, 9SFV, 9SFJ). Templates for template picking were generated using the MK-bound dataset (in nanodiscs). The same templates were used for processing of all other datasets.

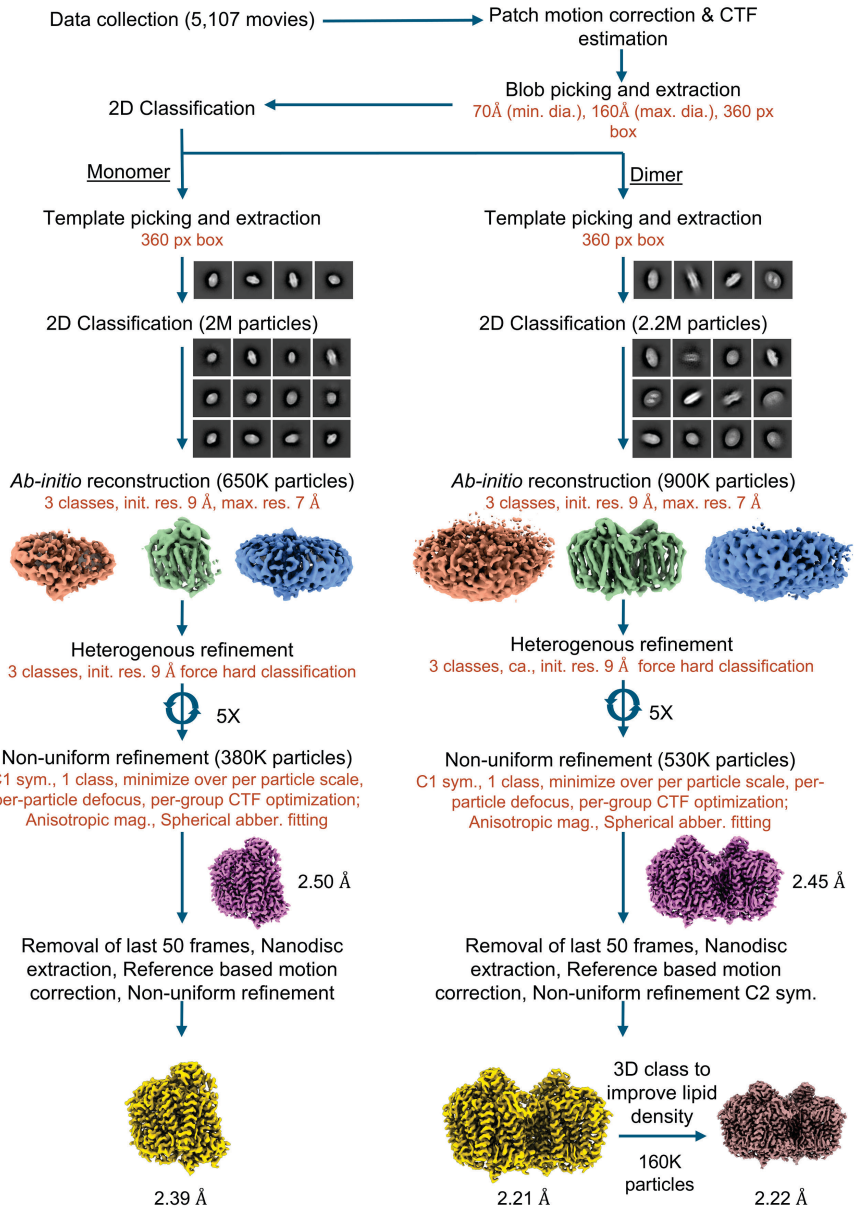


Figure S3.2: Cryo-EM processing of the *Ecbd* MK bound^{closed} structure (9SFF, 9RZV). Templates for template picking were generated using the MK-bound dataset (in nanodiscs) as shown in Fig. S1. The same templates were used for processing of all other datasets.

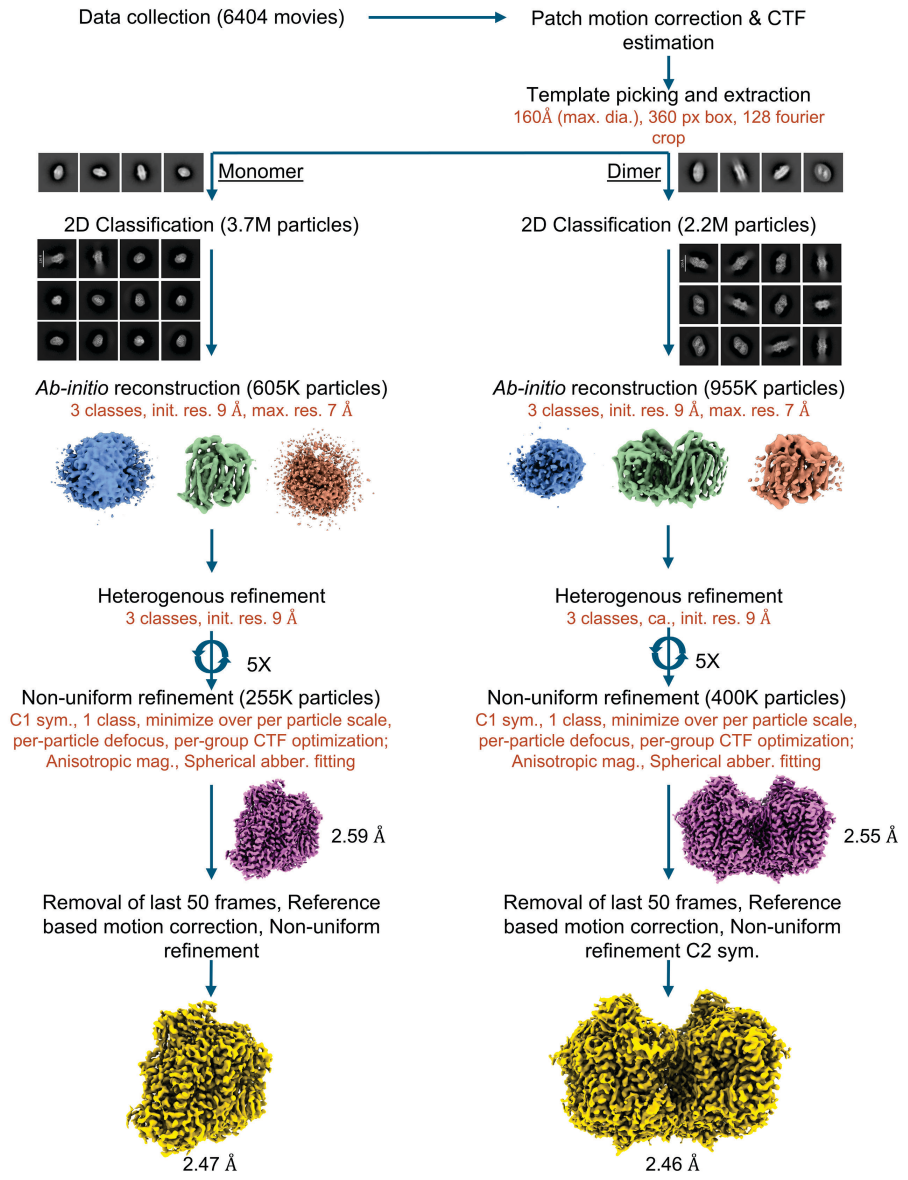


Figure S3.3. Cryo-EM processing of the Aurachin D bound *Ecbd* structures (9SFH, 9SEJ). Templates for template picking were generated using the MK-bound dataset (in nanodiscs) as shown in Fig. S1. The same templates were used for processing of all other datasets.

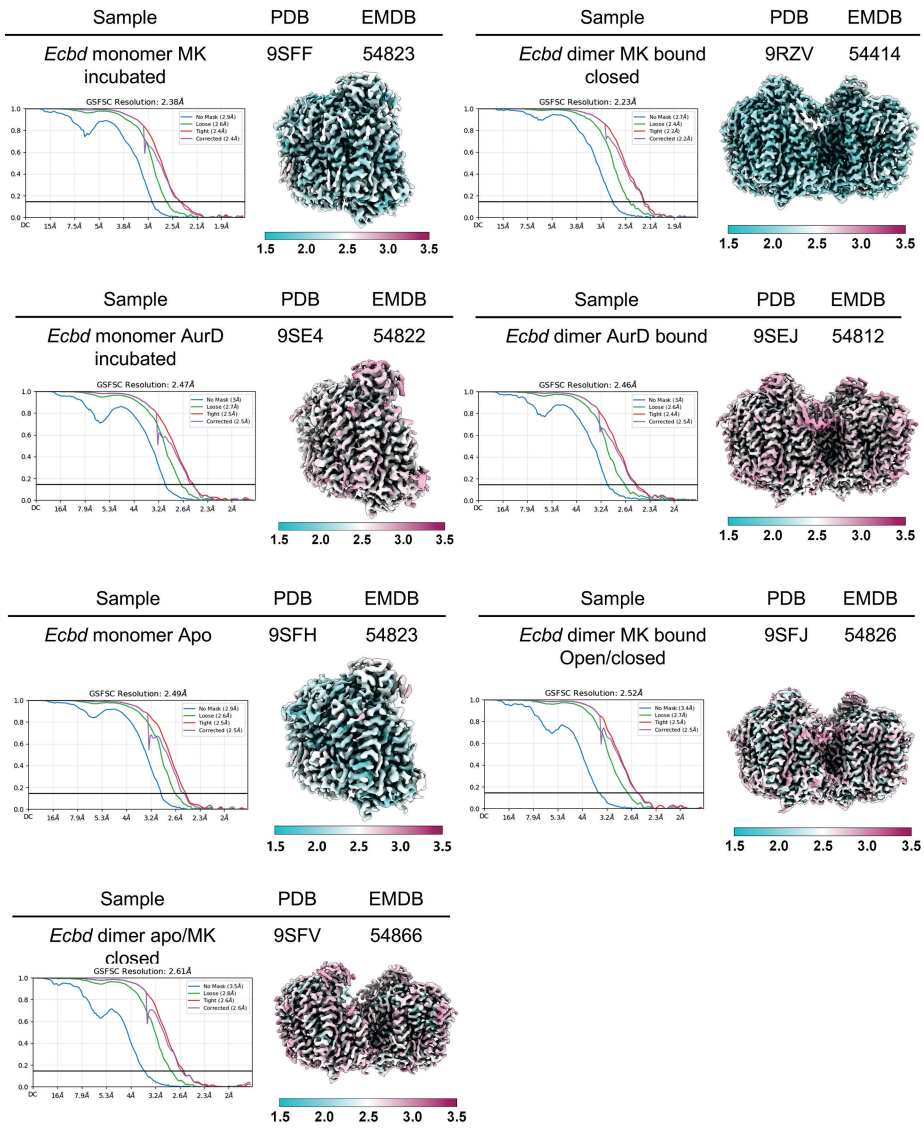


Figure S3.4: GSFSC curves and local resolution estimates

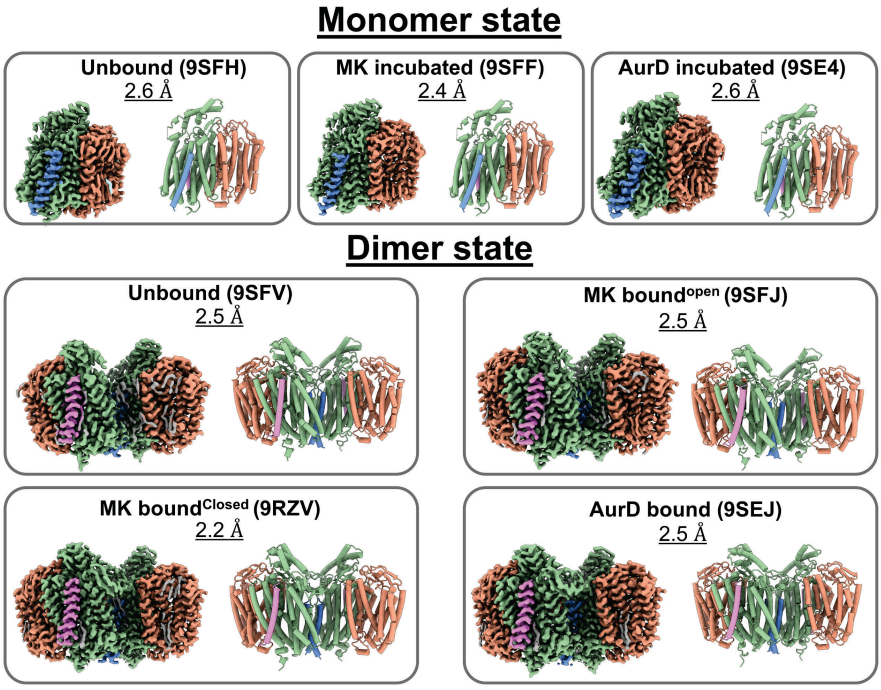


Figure S3.5. Overview of cryo-EM structures solved in this study

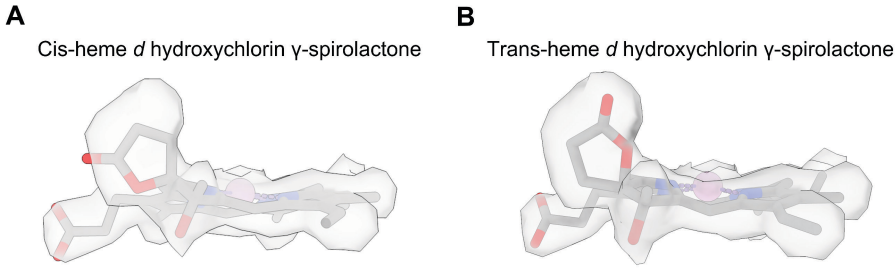


Figure S3.6. Fitting of the heme density with (**A**) cis heme *d* hydroxychlorin γ-spirolactone or (**B**) trans heme *d* hydroxychlorin γ-spirolactone.

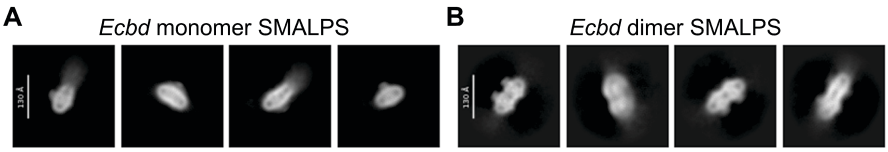


Figure S3.7. 2D classes of *Ecbd* after SMALP isolation (**A**) 2D classes of the *Ecbd* monomer (**B**) 2D classes of the *Ecbd* dimer showing of both oligomeric states *in vivo.*

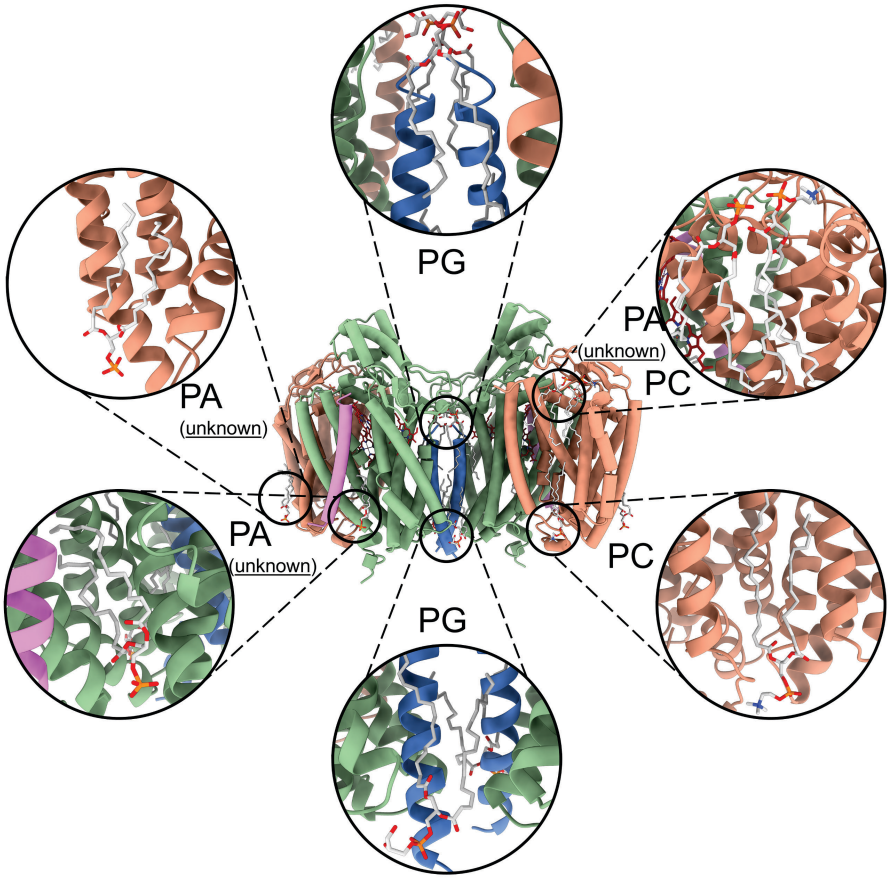


Figure S3.8. Lipids bound peripherally and to the interface of the *Ecbd* dimer. Lipids with unclear headgroup densities are modelled as phosphatidic acid (PA).

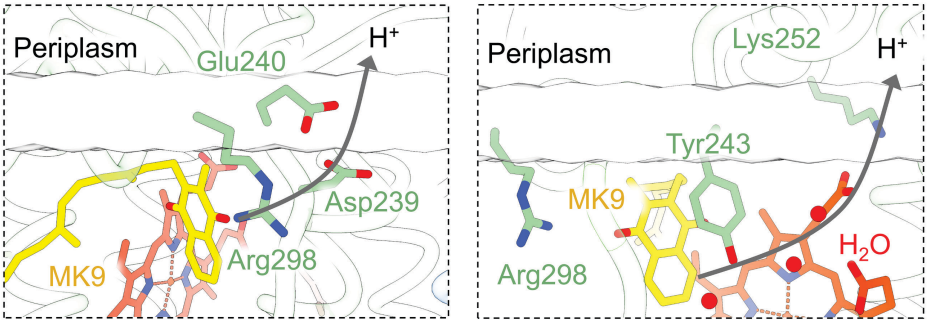


Figure S3.9. Putative proton transfer routes from the quinol oxidation site towards the periplasm. One route transfers past the Asp239 Glu240 pair near the quinol oxidation site. The other route transfers via structures water molecules towards Lys252 at the membrane interface.

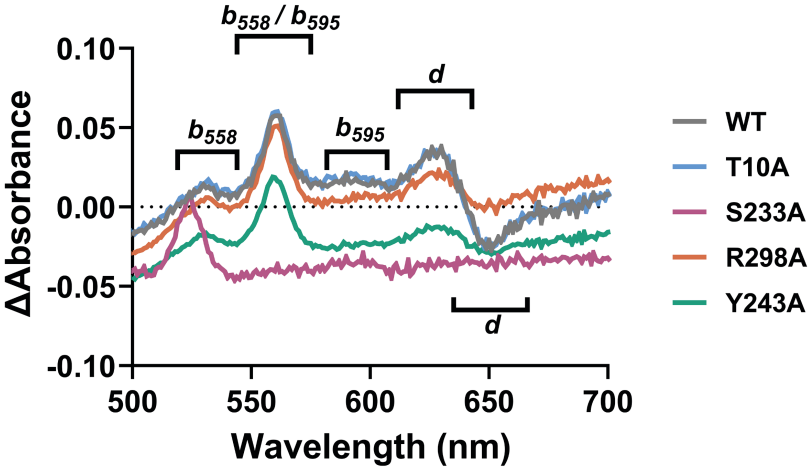


Figure S3.10. Reduced minus oxidized spectra of the *Ecbd* WT and the Y234A, R298A, T10A, S233A mutants. The data was normalized to the Soret band (415 nm) of the oxidized spectrum.

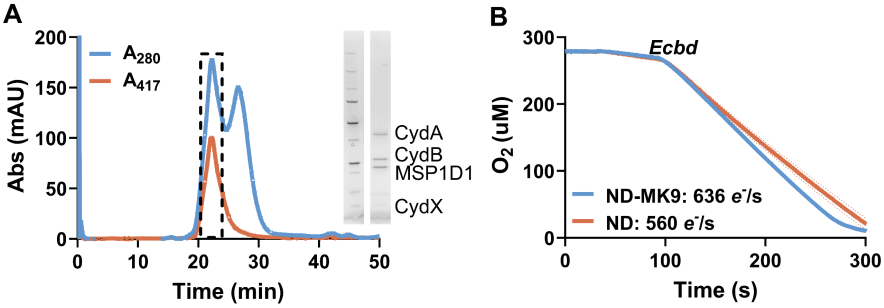
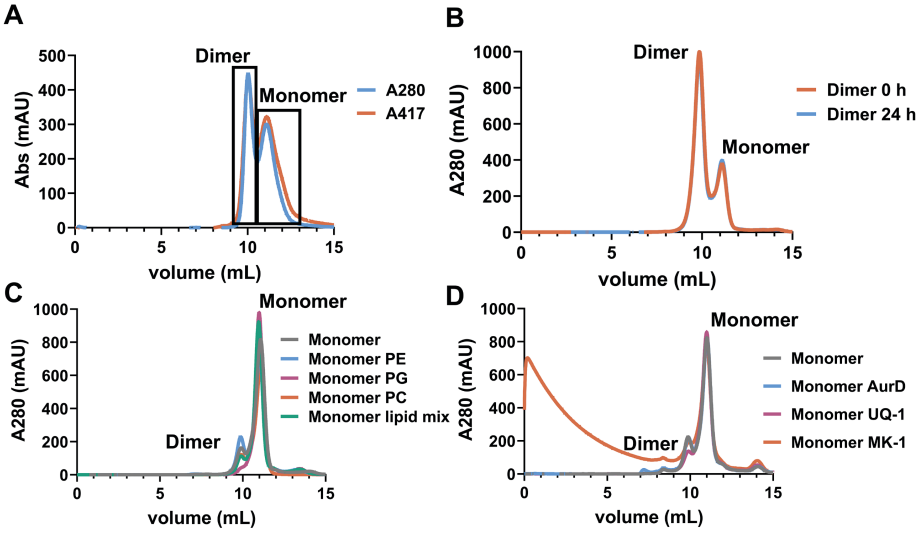


Figure S3.11. *Ecbd* reconstitution in nanodiscs. (**A**) Size exclusion of *Ecbd* nanodiscs. (**B**) Activity of *Ecbd* nanodiscs with either MK or UQ.



E

	Dimer peak Mw (kDa)	Monomer peak Mw (kDa)
Dimer 0 h	379.5	222.2
Dimer 24 h	380.4	216.1
Monomer	346.4	215.9
Monomer_Lipid Mix	407.9	220.8
Monomer_PE	669.9	269.4
Monomer_PG	-	215.5
Monomer AurD	865.6	296.3
Monomer UQ-1	368.8	227.5
Monomer MK-1	467.7	240.6

Figure S3.12. *Ecbd* reconstitution in nanodiscs. (**A**) SEC of the Strep purified *Ecbd* in LMNG on a superdex 200 column, enriching monomer and dimer *Ecbd* samples. (**B**) Stability of the SEC-purified *Ecbd* dimer (boxed in panel (**A**)) in detergent on SEC MALS. (**C**) SEC-MALS traces of SEC-purified *Ecbd* monomers (boxed in panel (**A**)) showing stable oligomeric state upon incubates with lipids or (**D**) incubation with quinones and Aurachin D (AurD). The addition of MK results in a decreasing baseline due to its absorption at 280 nm. (**E**) Mass determination by SEC MALS of the monomeric and dimeric *Ecbd* peaks.

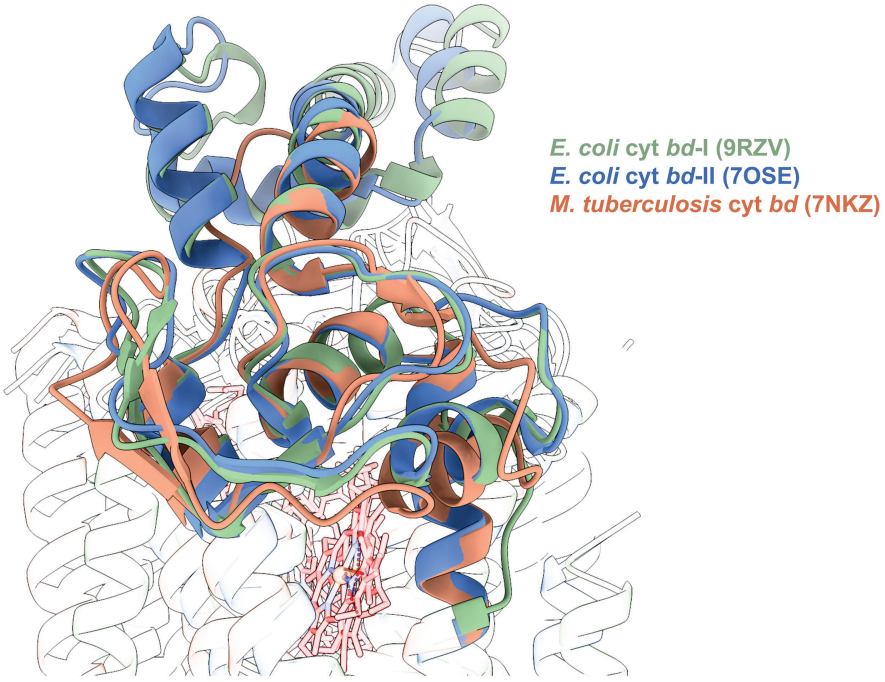


Figure S3.13. Overlay of the Q-loop fold found in the *E. coli* cyt *bd*-I MK bound state (9RZV), *E. coli* cyt *bd*-II AurD bound state (7OSE), and *M. tuberculosis* cyt *bd* (7NKZ).

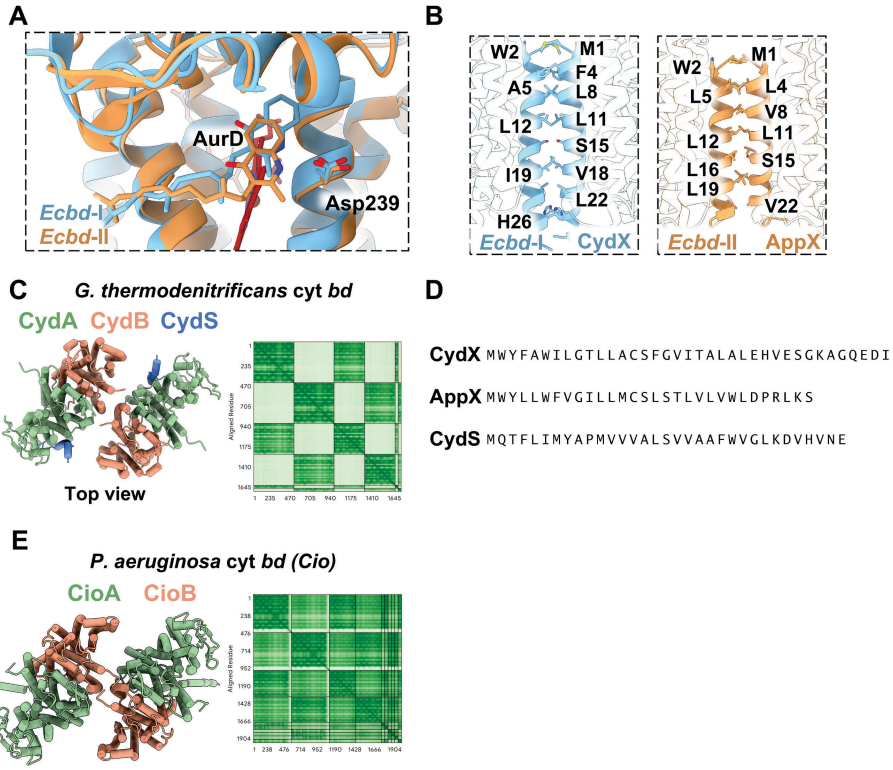


Figure S3.14. Comparison of AurD binding and the dimer interface (**A**) binding of AurD to *Ecbd*-I and *Ecbd*-II (7OSE) (**B**) Dimer interface of *Ecbd*-I CydX and *Ecbd*-II AppX (**C**) Predicted *G. thermodenitrificans* cyt *bd* dimer using AlphaFold 3, indicating Cyd S does not stabilize dimer formation. (**D**) sequence comparison of *E. coli* CydX, AppX and *G. thermodenitrificans* CydS. (**E**) Predicted *P. aeruginosa* cyt *bd* dimer using AlphaFold 3, indicating dimer formation formation via interactions of CydB.

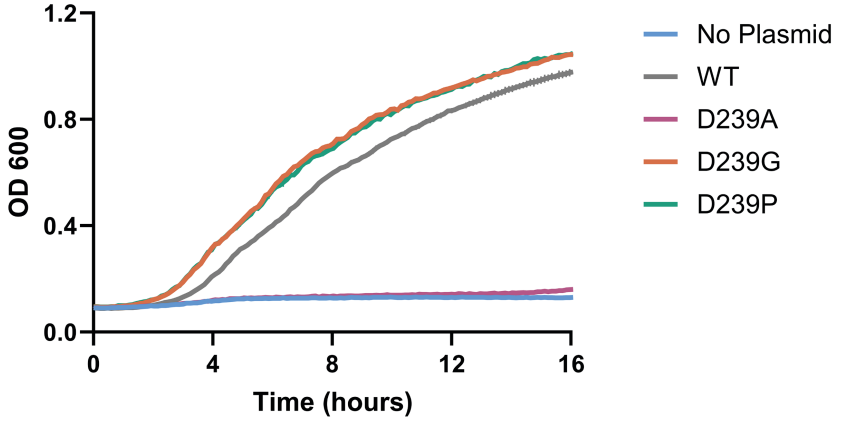


Figure S3.15. Growth curves of the MB43 ΔcydA knockout strain supplemented with *Ecbd*WT or its $D239^{CydA}$ mutants

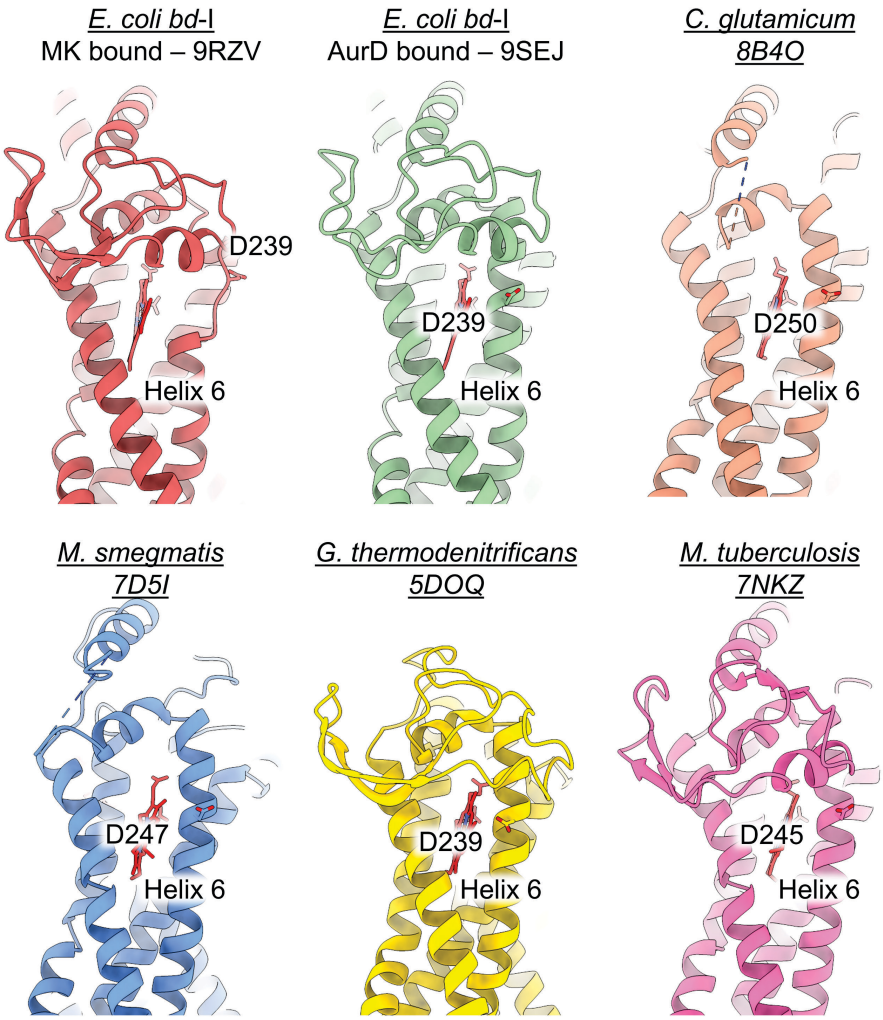


Figure S3.16. Overview of the helical states of cyt *bd* oxidases. The short Q-loop *bd* oxidases represent the helical fold of helix 6, as in the AurD inhibited state of *E. coli* cytochrome *bd*-I

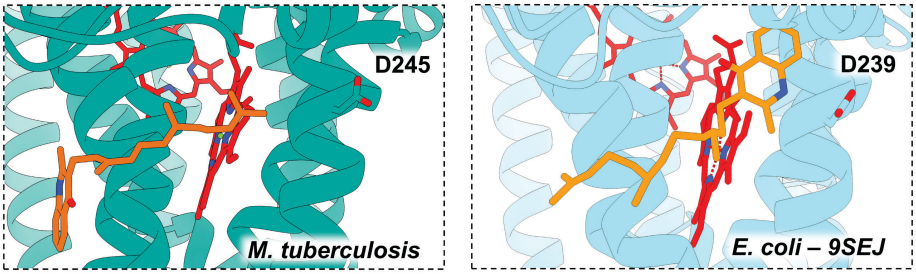


Figure S3.17. Comparison of the predicted binding pose of Aurachin D in *M. tuberculosis* cytochrome *bd* using AutoDock Vina[178,179] via Swissdock[180,181], with the cryo-EM structure of *Ecbd* bound to Aurachin D (9SEJ).

Table S3.1. Cryo-EM data collection, refinement and validation statistics

	Ecbd monomer Unbound (EMDB-54823) (PDB 9SFH)	*Ecbd* monomer MK incubated (EMDB-54822) (PDB 9SFF)	*Ecbd* monomer AurD incubated (EMDB-54801) (PDB 9SE4)	*Ecbd* dimer MK bound Closed (EMDB-54414) (PDB 9RZV)	*Ecbd* dimer MK bound-open/closed (EMDB-54826) (PDB 9SFJ)	*Ecbd* dimer unbound/MK closed (EMDB-54866) (PDB 9SFV)	*Ecbd* dimer AurD (EMDB-54812) (PDB 9SEJ)
Data collection and processing							
Magnification	130,000	105,000	130,000	105,000	130,000	130,000	130,000
Voltage (kV)	200	300	200	300	200	200	200
Electron exposure (e–/Å^2)	100	100	100	100	100	100	100
Defocus range (μm)	-0.8 – -2.0	-1.0 – -2.2	-0.8 – -2.0	-1.0 – -2.2	-0.8 – -2.0	-0.8 – -2.0	-0.8 – -2.0
Pixel size (Å)	0.880	0.836	0.880	0.836	0.880	0.880	0.880
Symmetry imposed	C1	C1	C1	C2	C1	C1	C2
Initial particle images (no.)	6,873,607	2,979,789	3,721,318	3,289,126	6,873,607	6,873,607	2,009,440
Final particle images (no.)	764,760	380,310	399,575	530,094	224,083	152,474	255,127
Map resolution (Å)	2.49	2.39	2.47	2.23	2.52	2.61	2.47
FSC threshold	0.143	0.143	0.143	0.143	0.143	0.143	0.143
Map resolution range (Å)	2.46-2.6	2.39-2.51	2.47-2.56	2.21-2.28	2.52-2.58	2.5-2.56	2.45-2.51
Refinement							
Initial model used (PDB code)	6RKO			Alphafold			

Model resolution (Å)	2.6	2.4	2.5	2.2	2.4	2.5	2.3
FSC threshold	0.5	0.5	0.5	0.5	0.5	0.5	0.5
Map sharpening *B* factor (Å^2)	-60	-60	-60	-40	-60	-60	-60
Model composition							
Non-hydrogen atoms	7492	7492	7492	16307	15464	15412	15975
Protein residues	892	892	892	1902	1902	1858	1902
Ligands	2 HEM, 1 A1JN4, 3 LPP, 1 UQ8, 1 OXY	2 HEM, 1 A1JN4, 3 LPP, 1 MQ9, 2 POV, 1 OXY	2 HEM, 1 A1JN4, 3 LPP, 1 UQ8, 1 OXY	4 HEM, 2 A1JN4, 6 LPP, 4 MQ9, 4 PGT, 4 POV, 2 UQ8, 2 OXY	4 HEM, 2 A1JN4, 6 LPP, 2 MQ8, 4 UQ8, 2 OXY	4 HEM, 2 A1JN4, 6 LPP, 1 MQ8, 4 UQ8, 2 OXY	4 HEM, 2 A1JN4, 4 LPP, 2 oNI, 2 PGT, 2 POV, 4 UQ8, 2 OXY
Water	32	32	32	77	10	10	98
***B* factors (Å^2)**							
Protein	68.40	79.60	63.40	53.92	97.41	124.62	78.28
Ligand	52.36	87.37	50.36	62.80	100.32	122.41	77.50
R.m.s. deviations							
Bond lengths (Å)	0.003	0.003	0.003	0.004	0.004	0.004	0.004
Bond angles (°)	0.805	0.703	0.806	0.749	1.460	1.140	1.47
Validation							
MolProbity score	1.60	1.39	1.58	1.31	1.40	1.32	1.37
Clashscore	7.79	5.68	7.51	2.01	5.05	2.29	4.28
Poor rotamers (%)	1.5	0.55	1.64	0.26	1.32	1.12	0.58
Ramachandran plot							
Favored (%)	97.85	97.84	97.96	99.26	97.83	97.61	97.93

Allowed (%)	2.04	2.16	2.04	0.96	2.17	2.39	1.96
Disallowed (%)	0.11	0	0	0.05	0	0	0.11

Table S3.2. Mutagenesis primers

Primer	Sequence
Ecbd.A S233A Fw	atggctgctgttctggctgttattgttctgggt
Ecbd.A S233A Rv	acccagaacaataacagccagaacagcagccat
Ecbd.A D239A Fw	tctgttattgttctgggtgccgaatccggctacgaaatgggc
Ecbd.A D239A Rv	gcccatttcgtagccggattcggcacccagaacaataacaga
Ecbd.A D239G Fw	tctgttattgttctgggtggcgaatccggctacgaaatgggc
Ecbd.A D239G Rv	gcccatttcgtagccggattcgccacccagaacaataacaga
Ecbd.A D239P Fw	attgttctgggtccagaatccggctac
Ecbd.A D239P Rv	gtagccggattctggacccagaacaat
Ecbd.A Y243A Fw	ctgggtgacgaatccggcgccgaaatgggcgacgtgcag
Ecbd.A Y243A Rv	ctgcacgtcgcccatttcggcgccggattcgtcacccag
Ecbd.A R298A Fw	ctgggcatcattgcaacggcatccgtggataccccggtt
Ecbd.A R298A Rv	aaccggggtatccacggatgccgttgcaatgatgcccag
Ecbd.X T10A Fw	gcatggattctgggagctcttcttgcctgttcg
Ecbd.X T10A Rv	cgaacaggcaagaagagctcccagaatccatgc
Ecbd Gibson Fwd	gcccgaaaggaagctgagtt
Ecbd Gibson Rev	aactcagcttcctttcgggc